BMC Women's Health

RESEARCH

Open Access

Metabolism-associated marker gene-based predictive model for prognosis, targeted therapy, and immune landscape in ovarian cancer: an integrative analysis of single-cell and bulk RNA sequencing with spatial transcriptomics

Lele Ling[1,2†], Bingrong Li[1†], Boliang Ke[4,5†], Yinjie Hu[1], Kaiyong Zhang[1], Siwen Li[1], Te Liu[3*], Peng Liu[1*] and Bimeng Zhang[1*]

Abstract

Background Ovarian cancer (OC) is a formidable gynecological tumor marked with the highest mortality rate. The lack of effective biomarkers and treatment drugs places a substantial proportion of patients with OC at significant risk of mortality, primarily due to metastasis. Glycolysis metabolism, lipid metabolism, choline metabolism, and sphingolipid metabolism are closely intertwined with the occurrence and progression of OC. Thus, it is of utmost significance to identify potent prognostic biomarkers and delve into the exploration of novel therapeutic drugs and targets, in pursuit of advancing the treatment of OC.

Methods Single-cell RNA sequencing (scRNA-seq) data related to OC were analyzed using AUCell scores to identify subpopulations at the single-cell level. The "AddModuleScore" function of the "Seurat" package was adopted to score and select marker genes from four gene sets: glycolysis metabolism, lipid metabolism, choline metabolism, and sphingolipid metabolism. A prognostic model for metabolism-related genes (MRGs) was constructed and validated using OC-related marker genes selected from bulk RNAseq data. The MRG-based prognostic model was further utilized for functional analysis of the model gene set, pan-cancer analysis of genomic variations, spatial transcriptomics analysis, as well as GO and KEGG enrichment analysis. CIBERSORT and ESTIMATE algorithms were utilized for assessing the immune microenvironment of TCGA-ovarian serous cystadenocarcinoma (OV) samples. Furthermore, the Tracking

†Lele Ling, Bingrong Li and Boliang Ke contributed equally to this work and shared the first authorship.

*Correspondence:
Te Liu
liute1979@shutcm.edu.cn
Peng Liu
lpeason@163.com
Bimeng Zhang
Pjzhtiger08@aliyun.com
Full list of author information is available at the end of the article

Tumor Immunophenotype (TIP) database was employed to examine the anti-cancer immune response in patients with OC. To gain a more in-depth understanding of the process, the frequency of somatic mutations and different types of mutated genes were visualized through the somatic mutation profile of the TCGA database. Moreover, the benefits of immune checkpoint inhibitor (ICI) therapy in individuals with OC were predicted in the TIDE database. In addition, the CMap database was used to predict small-molecule drugs for the treatment of OC. Furthermore, immunohistochemistry, RT-qPCR, CCK-8, Transwell assay, and in vivo tumor xenograft experiments were conducted to validate the prognostic ability of the MRG Triggering Receptor Expressed on Myeloid Cells-1 (TREM1) in OC.

Results Monocytes were selected using AUCell scoring, and two subpopulations of monocytes, marked by the expression of $C1QC^+$ tumor-associated macrophages (TAMs) and $FCN1^+$ resident tissue macrophages (RTMs), were identified as marker genes for OC. Subsequently, a prognostic model consisting of 12 MRGs was constructed and validated. Genomic exploration of the prognostic model unveiled an array of biological functions linked with metabolism. Furthermore, copy number variation (CNV), mRNA expression, single nucleotide variation (SNV), and methylation were significantly different across diverse tumors. Analysis of the TIP database demonstrated that the low-risk group, as determined by the MRG-based prognostic model, exhibited significantly higher anti-cancer immune activity relative to the high-risk group. Furthermore, predictions from the TIDE database revealed that individuals in the high-risk group were more prone to immune evasion when treated with ICIs. The resulting data identified candesartan and PD-123319 as potential therapeutic drugs for OC, possibly acting on the target *ATGR2*. In vitro and in vivo experiments elucidated that the targeted downregulation of TREM1 effectively inhibited the proliferation and migration of OC cells.

Conclusion The MRG-based prognostic model constructed through the combined analysis of glycolysis metabolism, lipid metabolism, choline metabolism, and sphingolipid metabolism is potentially effective as a prognostic biomarker. Furthermore, candesartan and PD-123319 may be potential therapeutic drugs for OC, possibly acting on the target *ATGR2*.

Keywords Metabolism, Ovarian cancer, Biomarkers, Single-cell sequencing, Bulk RNA sequencing

Graphical Abstract

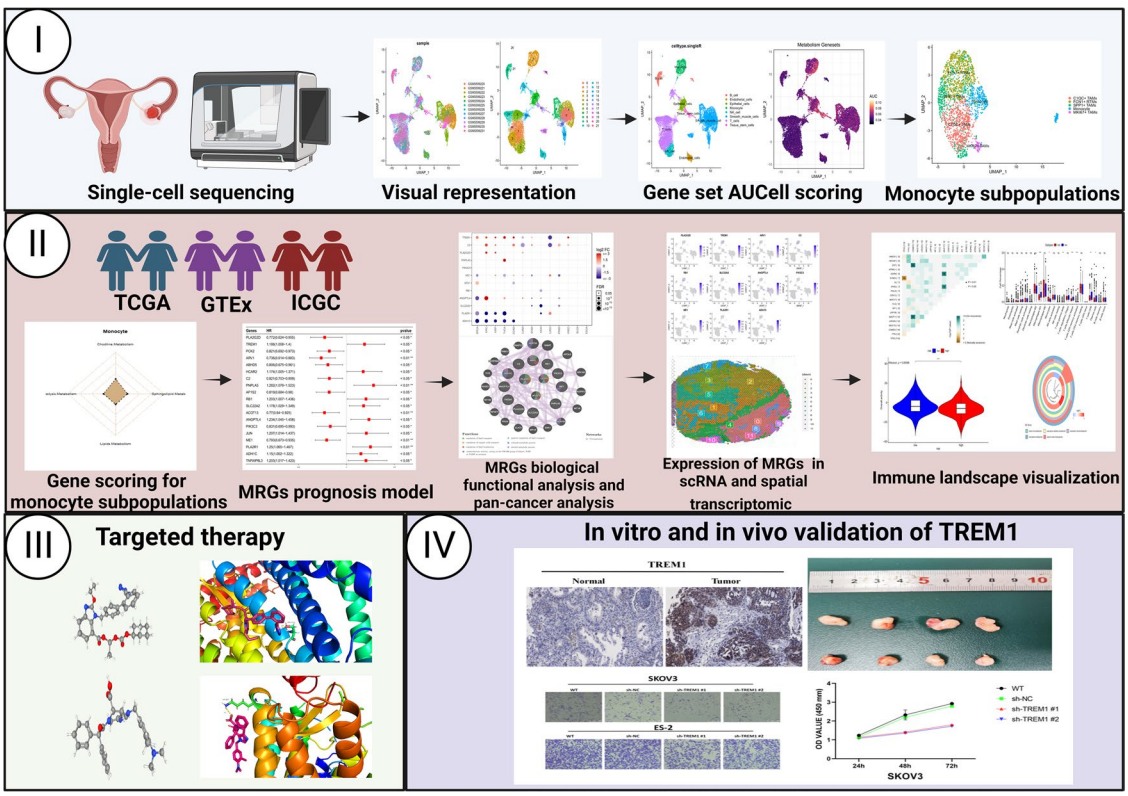

Introduction

Ovarian cancer (OC) remains the leading contributor to death among gynecological tumors worldwide. This can be attributed to a variety of factors, including the lack of effective screening methods, non-specific early symptoms, poorly defined biomarkers, limited treatment options, high recurrence rates, and high metastasis rates [1]. The conventional treatment for OC is surgical intervention combined with platinum-based and taxane-based chemotherapy, yet approximately 25% of patients experience recurrence within one month after chemotherapy [2, 3]. Recent years have witnessed notable strides in OC treatment, exemplified by the incorporation of anti-angiogenic agents and poly(ADP-ribose) polymerase inhibitors, which have contributed to the transformation of OC into a potentially manageable disease. Nonetheless, the overall survival (OS) rate of OC has exhibited limited improvement [4–6]. Given the lack of alternative therapeutic approaches aimed at facilitating the prognosis of individuals with OC, the majority of such patients ultimately succumb to metastasis. Therefore, it is imperative to develop effective biomarkers and construct predictive models to identify the risk of OC.

Tumor cell metabolism assumes a central role in governing both cancer progression and survival [7]. These metabolic processes influence the expression of specific genes and proteins integral to tumorigenesis, thus rendering metabolic reprogramming a notable hallmark of cancer. In this context, prevalent metabolic characteristics in cancer cells include aerobic glycolysis, lipid metabolism, and protein homeostasis controlled by intrinsic cellular mechanisms. These metabolic activities are further influenced by oncogenic mutations and stimulated through intricate transcriptional regulatory networks [8–10]. Additionally, the tumor microenvironment (TME) undergoes metabolic reprogramming to fulfill the energy demands of tumor cells, highlighting another prominent feature [11]. Recently, increasing studies have exhibited the high complexity of tumor metabolism [10]. The acquired data are evidence of the intricacy of the process, noting that tumor metabolism is not confined to a single reprogramming process but is likely regulated by multiple metabolic pathways. Therefore, the comprehensive assessment of multiple metabolic processes underscores their significance.

The emergence of single-cell technologies has enhanced our understanding of OC by enabling the single-cell assessment of patient samples. Single-cell RNA sequencing (scRNA-seq) allows for the identification of different cell subpopulations and recognition of key factors contributing to tumor heterogeneity and provides essential information to further elucidate mechanisms underlying OC progression [12]. In this study, an innovative investigation was undertaken, entailing a joint analysis of four closely related metabolic processes in OC cells: glycolysis metabolism, lipid metabolism, choline metabolism, and sphingolipid metabolism. Based on OC-related scRNA data, AUCell scoring was applied to assess the four metabolic processes in monocyte subpopulations and evaluate the scores of these metabolic processes in these subpopulations using Seurat scoring functions. Moreover, differentially expressed genes (DEGs) were selected based on the scored marker genes to construct a metabolism-related gene (MRG)-based prognostic model. Functional analysis, pan-cancer analysis of genomic variations, and spatial transcriptomic data analysis were conducted using the prognostic model gene set. Additionally, small molecule drugs for treating OC were predicted based on the differential prediction of a high-risk group (HRG) and a low-risk group (LRG). Furthermore, in vitro and in vivo experiments were performed to validate the impact of Triggering Receptor Expressed on Myeloid Cells-1 (*TREM1*), a metabolism-related prognostically significant gene, on OC progression and prognosis (Graphical abstract).

Materials and methods

Acquisition and screening of expression profiling data

RNA-seq data (COUNT and FPKM) for TCGA-ovarian serous cystadenocarcinoma (OV) were acquired from The Cancer Genome Atlas (TCGA) Genomic Data Commons (GDC) database (https://portal.gdc.cancer.gov/). The survival information of the TCGA pan-cancer Clinical Data Resource (TCGA-CDR) was also downloaded [13]. Cancer tissue samples with available prognostic information were selected, resulting in a total of 376 tumor tissue samples included for subsequent analysis and model construction.

From the GTEx database (https://www.gtexportal.org/), RNA-seq data for normal ovaries were downloaded as controls, comprising a total of 88 normal samples, for subsequent analysis. The OV-AU dataset and associated clinical data were acquired from the International Cancer Genome Consortium (ICGC) database (https://dcc.icgc.org/), with a final inclusion of 93 tumor samples for subsequent model validation. Ovary scRNA-seq data were accessed at the GEO database, specifically the GSE184880 dataset, which consisted of 5 normal samples and 7 tumor samples.

Acquisition of gene sets

A total of 76 genes were obtained from the provided choline MRG set. The MSigDB database (https://www.gsea-msigdb.org/gsea/msigdb) was searched for "glycolysis metabolism,""lipid metabolism,"and"sphingolipid metabolism" to download gene sets associated with glycolysis, lipid, and sphingolipid metabolism.

scRNA data analysis

The scRNA data were analyzed using "Seurat" (v4.3.0, https://cran.r-project.org/web/packages/Seurat/index.html) [14]. The data underwent quality control, dimensionality reduction using principal component analysis (PCA) as well as batch correction using Harmony. Furthermore, clustering analysis was conducted using 20 principal components, with the resolution parameter for cell clustering set at 0.8.

Cell subpopulation annotation

Based on the reference data from the HumanPrimaryCellAtlasData platform, the "singleR" package (v2.0.0, https://www.bioconductor.org/packages/release/bioc/html/SingleR.html) [15] was employed to perform cell subtype annotation for the aforementioned cell subpopulations.

Gene set AUCell scoring

"AUCell" package is a computational method designed to evaluate the activity of gene sets at the single-cell level by calculating the Area Under the Curve (AUC) of the recovery curve for each gene set within individual cells. This approach ranks genes by their expression levels in each cell and quantifies the enrichment of predefined gene sets (e.g., pathways, regulatory modules, or cell-type signatures) by measuring the cumulative expression of genes in the set relative to the overall expression profile. Therefore, we employed the "AUCell" package (v1.20.2, https://bioconductor.org/packages/release/bioc/html/AUCell.html) [16] was employed to perform AUCell scoring for all cells based on the aforementioned gene set after removing duplicates.

Cellular reclustering analysis

Monocyte-related data were extracted for cell reclustering analysis and underwent PCA for dimensionality reduction. For this analysis, twenty principal components (PCs) were selected, and reclustering was conducted with a resolution parameter set at 0.3. The annotation of monocyte subtypes was manually conducted as previously described [17].

Gene scoring

To evaluate the activity levels of specific functional gene sets, we utilize the built-in AddModuleScore algorithm from the"Seurat"package [14]: This method calculates the average expression value of the target gene set, adjusts for the background distribution of gene expression levels, and ultimately generates a composite score reflecting the activity of the gene module. Therefore, we employed the AddModuleScore scoring function to evaluate the activity scores of four metabolism-related gene sets (choline metabolism, glycolysis metabolism, lipid metabolism, and sphingolipid metabolism) in monocyte subpopulations.

Differential expression analysis

Differential expression analysis was performed between tumor and normal samples using R "DESeq2" (v1.36.0, https://www.bioconductor.org/packages/release/bioc/html/DESeq2.html). The threshold for selecting differentially expressed genes (DEGs) was set at a false discovery rate (FDR) (adjusted p value) <0.05 and a fold change ($\log_2$FC) >0.58 (equivalent to $\log_2 1.5$). Subsequently, the DEGs were obtained by intersecting the results with four gene sets and marker genes of two macrophage subpopulations.

Protein–protein interaction (PPI) network of DEGs

The PPI network of DEGs was established utilizing the STRING database (https://cn.string-db.org/). A screening threshold of combined_score >0.95 was applied, and the PPI network was built using Cytoscape (v 3.9.1).

Data partitioning for training and external validation sets

Tumor samples from TCGA-OV dataset were randomly categorized into training (60%) and testing (40%) sets. The data acquired from the ICGC database were utilized as an external validation set due to the unavailability of suitable models from GEO data. The training set was utilized for subsequent modeling, while the external validation set was used to validate and evaluate the model. To establish uniformity, FPKM transformation was applied to the original data on both TCGA-OV and ICGC data, followed by $\log_2$ transformation and normalization to ensure that they followed the same distribution and to eliminate the influence of different batches before modeling.

Identification of prognostically significant genes

In the training set, the DEGs obtained previously were combined with clinical survival prognosis information to perform univariate Cox regression analysis using the "survival" package (v3.4–0, https://mran.microsoft.com/web/packages/survival/index.html) [6]. Furthermore, genes strongly linked with OS prognosis were selected using a threshold of $p<0.05$.

Development and validation of the prognostic characteristic model

Based on the genes significantly associated with survival prognosis as mentioned earlier, the LASSO Cox regression model from the "glmnet" package [7] in R (v2.0–18, https://cran.r-project.org/web/packages/glmnet/index.html) was further utilized. The model incorporated

survival prognosis information from the training set samples and the gene expression values in each sample. A tenfold cross-validation analysis was employed to further select gene combinations pertinent to prognosis. Subsequently, based on the LASSO regression coefficients of the genes and their expression levels in the samples of the TCGA-OV training set, the following RiskScore model was constructed, with RiskScore calculated as follows:

$$RiskScore = \sum \beta gene \times Expgene$$

wherein, βgene denotes the LASSO regression coefficient of the gene and Expgene denotes the relative expression level of the gene.

Furthermore, to examine the accuracy of the model, the RiskScore values for every sample in the testing set and the ICGC external validation set were quantified utilizing the same regression coefficients as per the RiskScore calculation formula. Afterward, with the median RiskScore value as a threshold, all samples in the testing set and external validation set were allocated into High_Risk (RiskScore ≥ median RiskScore value) and Low_Risk (RiskScore < median RiskScore value) sample groups. The association between the two groups and the actual survival prognosis were analyzed utilizing the Kaplan–Meier (KM) curve method from the "survival" package in R [6]. Additionally, 1-, 3-, and 5-year survival was assessed by plotting the receiver operating characteristic (ROC) curves utilizing the "survivalROC" package [8] (v1.0.3, https://mran.microsoft.com/web/packages/survivalROC/index.html), with subsequent quantification of the respective area under the curve (AUC) values.

Construction of nomograms

Through the R"survival"package, the RiskScore prognostic model and clinical information were analyzed via Cox analyses (univariate and multivariable) to determine prognosis-linked independent factors. The independent prognostic factors were employed to construct nomograms using the"rms"package in R (v 6.3–0, https://mran.microsoft.com/web/packages/rms/index.html). Based on these independent prognostic factors, a clinical risk model was established using multivariable Cox regression analysis, and the clinical risk values (nomoScore) were calculated for all samples in the TCGA-OV dataset. These samples were then classified into two groups: High_nomoRisk (nomoScore ≥ median nomoScore value) and Low_nomoRisk (nomoScore < median nomoScore value). The variance in prognosis was comparatively assessed across the two groups using KM curves. The AUC values for 1-, 3-, and 5-year survival were quantified to evaluate the clinical risk model. This model was further assessed using calibration curve analysis with the"rms"package and decision curve analysis (DCA) using the"dcurves"package (v 0.3.0, https://mran.microsoft.com/web/packages/dcurves/index.html).

Functional analysis of model genes

The GeneMANIA database (http://genemania.org/) was employed to generate genes that exhibited similar functional characteristics to the model genes and to predict their biological functions.

Pan-cancer analysis of genomic variations in model genes

Based on the GSCALite database, an in-depth analysis was performed on the mRNA expression, single nucleotide variation (SNV), methylation, and copy number variation (CNV) of the key genes related to the model. Additionally, the correlation between mRNA expression and CNV, as well as methylation, was also investigated.

Spatial transcriptomic data analysis

The human OC-related spatial transcriptomic data was accessed at the 10X GENOMICS database (https://www.10xgenomics.com/). The data were from formalin-fixed, paraffin-embedded (FFPE) samples and were obtained using the Spatial Gene Expression Dataset generated by Space Ranger 1.3.0. The "Seurat" package was employed to analyze and explore the spatial transcriptomic data, followed by PCA for dimensionality reduction and cluster analysis using 20 PCs. The expression of model genes was further investigated and validated in the spatial transcriptomic data.

Gene Ontology (GO) and Kyoto Encyclopedia of Genes and Genomes (KEGG) enrichment analysis

The R package "DESeq2" was employed to identify DEGs between the HRG and LRG, and a volcano plot was established to visualize the data. The R package "clusterProfiler" (v 4.7.1, https://github.com/YuLab-SMU/clusterProfiler) was utilized for GO functional and KEGG pathway enrichment analyses of the DEGs.

Analysis of the immune microenvironment (IME) in HRG (High Risk Group) and LRG (Low Risk Group)

To further explore the IME in the HRG and LRG, algorithms, including ESTIMATE and CIBERSORT (22 immune cell types), were utilized in the analysis. The TME score and immune cell scores were calculated using these algorithms. Furthermore, the Wilcoxon rank-sum test was employed to evaluate the variance in TME score and immune cell composition.

For this analysis, two algorithms were employed to assess the IME status of TCGA-OV samples:

1. CIBERSORT (https://cibersortx.stanford.edu/) [18, 19] was applied to examine the relative proportions of 22 immune cell types based on the expression levels of tumor samples. CIBERSORT is a deconvolution tool based on the principles of linear support vector regression, which estimates the composition of immune cell subtypes from the expression matrix. Herein, both relative mode and absolute mode were selected for analysis.
2. Estimation of STromal and Immune cells in MAlignant Tumour tissues using Expression data (ESTIMATE) [19] is based on single-sample gene set enrichment analysis (ssGSEA). It enables the deduction of the infiltrating immune cells and stromal cells, as well as the calculation of stromal and immune scores and the content of tumor cells, using the transcriptional profiles of cancer samples. This algorithm allows for the quantification of the proportions or abundance of immune, stromal, and tumor cells that are relevant to the TME in the tumor tissue.

The expression profiles of immune checkpoint genes (ICGs) were extracted to compare the differential expression of ICGs between HRG and LRG. The TIP database (http://biocc.hrbmu.edu.cn/TIP/index.jsp) was employed to examine the anti-cancer immune response in individuals with OC. The Wilcoxon rank-sum test was employed to assess the variance in anti-cancer immune response scores across the HRG and LRG.

Analysis of somatic cell mutations

Somatic cell mutation profiles of the TCGA database were visualized using the"maftools"package (v 2.14.0, https://bioconductor.org/packages/release/bioc/html/maftools.html) in R. To visually represent the distribution of the distinct types of mutated genes and the frequency of somatic cell mutations across the risk groups, a waterfall plot was developed [20].

Prediction of drug sensitivity and immunotherapy efficacy

The Genomics of Drug Sensitivity in Cancer (GDSC) database (https://www.cancerrxgene.org/) was employed to investigate the responsiveness of individual patients to chemotherapeutic drugs. The application of "pRRophetic" package in R (v 0.5, https://github.com/paulgeeleher/pRRophetic) was utilized to examine the half-maximal inhibitory concentration (IC_{50}) of the drug. Differences in drug sensitivity between HRG and LRG were compared using the Wilcoxon test.

The TIDE database (http://tide.dfci.harvard.edu/) was utilized for assessing the extent of the benefit of immune checkpoint inhibitor (ICI) therapy in patients with OC. The differences in TIDE scores between HRG and LRG were compared using the Wilcoxon test.

Molecular docking

The differential gene expression between HRG and LRG was uploaded to the CMap database (https://clue.io/) for the prediction of small-molecule drugs for OC treatment. The top five genes with the highest FC in upregulation were selected as target genes for drug screening. The gene and protein sequences, as well as annotation data, were acquired from The Universal Protein Knowledgebase database (UniProt; https://www.uniprot.org/). The main protein structures of major targets were accessed at the Protein Data Bank (PDB; http://www.rcsb.org). The 3D structures of small molecule drugs were acquired from PubChem (https://pubchem.ncbi.nlm.nih.gov/). The PyMOL software (PyMOL Molecular Graphics System; http://www.pymol.org) was adopted for the removal of water molecules and small molecule ligands, and the AutoDock Tools software (v 1.5.7) was utilized for docking the key targets with small molecule drugs. The binding activity of the compounds was assessed based on their docking scores, and the docking results were visualized.

Cell culture

The Shanghai Cell Bank, Chinese Academy of Sciences, was utilized to obtain the ovarian malignant cells lines SKOV3, ES-2, and Caov3 as well as the ovarian healthy epithelial cell line IOSE-80. We used complete medium RPMI 1640 (89% RPMI 1640(Gibco), 9% fetal bovine serum (Gibco), 1% Penicillin–Streptomycin Solution (Gibco)) for the culture and passaging of cells IOSE-80 and Caov3. Culture and passaging of SKOV3 and ES-2 using McCoy's 5 A complete medium (89% McCoy's 5 A (Gibco), 9% fetal bovine serum(Gibco), 1% Penicillin–Streptomycin Solution (Gibco)). All cell lines were cultured in a Thermo Fisher incubator at 37 ℃, 95% air, 5% CO_2, and 70% to 80% humidity.

Cell transfection

Short hairpin RNA (shRNA) targeting TREM1 (shTREM1) and a non-targeting scrambled control shRNA (shNC) were synthesized (Genechem). Cell were cultured in a culture dish until 70% confluence, followed by transfection of shRNA with the Lipo3000 transfection reagent. Wild-type, untransfected cells (WT) and shNC were used as comparators for shTREM1 knockdown experiments.

RT-qPCR

In summary, the total RNA was extracted utilizing the Trizol (EnzyArtisan, China) method, followed by the synthesis of cDNA through employment of the HyperScript

III 1 st Strand cDNA Synthesis Kit (EnzyArtisan, China). Ultimately, the RT-qPCR was executed with the QuantStudio 6 Flex real-time PCR system (Thermo Fisher, USA) by using 2× S6 Universal SYBR qPCR Mix (EnzyArtisan, China). Relative gene expression levels were calculated using the $2^{-\Delta\Delta Ct}$ method (ΔCt = Ct_genes-Ct_ GAPDH; ΔΔCt = ΔCt_all_groups—ΔCt_blank control_group). mRNA expression levels were normalized to those of GAPDH.

Human-TREM1-F-GAACTCCGAGCTGCAACTAAA.

Human-TREM1-R-TCTAGCGTGTAGTCACATTTCAC.

Human-GAPDH-F-AAGGTGAAGGTCGGAGTCAAC.

Human-GAPDH-R-GGGGTCATTGATGGCAACAATAR.

Transwell

Cells reaching 70–80% confluence were centrifuged and resuspended by DMEM medium (Gibco, USA). After counting, 200 µl of cells were inoculated into the upper chamber of a 24-well Transwell at 5×10^4 cells/well. Meanwhile, 500 µl of DMEM(Gibco, USA) complete medium containing 10% fetal bovine serum (FBS) was added to the lower chamber. After 24 h of incubation, the lower chamber was placed in a clean 24-well plate supplemented with 600 µl of 4% paraformaldehyde for 20–30 min, followed by staining with 0.1% crystal violet (Beyotime, China) for 5–10 min. After air-drying, the cells were observed under a microscope (Leica DMI8, GER) at 10 × magnification in five areas and counted.

CCK8

In brief, cells from each group were cultured in a 96-well plate and then with 10 µl CCK8 reagent (vazyme) at 24 h, 48 h and 72 h at 37 ℃ for 3 h, respectively. The percent suppression of cell proliferation was measured based on the optical density (OD) at 425 nm on a microplate reader. Inhibition rate = (ODexperiment—ODControl)/(ODControl – ODblank).

Tissue microarray

OC tissue microarray was supplied by Shanghai Outdo Technology Co. Ltd. (Shanghai, China).

It has been received approval from the Shanghai Outdo Biotech Ethics Committee.

Immunohistochemistry

The harvested tissue samples were fixed in formalin and paraffin-embedded with subsequent sectioning. The slides were dewaxed with xylene and hydrated with ethanol at different concentrations. The slides were boiled in antigen retrieval solution (1 mmol Tris–EDTA) (Sigma-Aldrich, St. Louis, MO, USA) for 15 min, with a subsequent 15-min incubation at room temperature for antigen retrieval. Each slide was incubated for 20 min with 100 µl of 5% BSA blocking solution (Sigma-Aldrich) at room temperature for the prevention of non-specific binding of antibodies. A 100 µl aliquot of rabbit anti-TREM1 antibody (#BF0084, Affinity, China) diluted at a ratio of 1:200 was added onto each slide and kept overnight at 4℃. The slides were rinsed thrice with PBS for 5 min and then incubated with 100 µl of labeled goat anti-mouse IgG (ab150113, Abcam, UK) at 37℃ for 30 min. The washing step was repeated with the same parameters, and the slides were then stained with a chromogen for 10 min, thoroughly rinsed with tap water, counterstained, dehydrated, permeabilized, and mounted.

In vivo tumorigenic experiment

This study used BALB/c nude mice to subcutaneously inject approximately 1× 106 logarithmically growing SKOV3 (pre-mixed with 100 µl PBS from Gibco, USA) that were transfected with sh-TREM1(n = 4) and WT (n = 4). At the end of a 30-day period, the mice were euthanized, and the in vivo tumors were collected. Tumor weight and volume were measured. Tumor volume (mm3) was measured as (ab2)/2, where a and b represent the longest axis (mm) and the shortest axis (mm), respectively. After the experiment, the mice were euthanized using the method of excessive inhalation of CO2. 8 BALB/c nude mice were obtained from the Experimental Animal Center of Shanghai General Hospital affiliated to Shanghai Jiao Tong University School of Medicine. Ethical approval of this animal experiment was granted by the Experimental Animal Center of Shanghai General Hospital affiliated to Shanghai Jiao Tong University School of Medicine (Approval number: (IACUC):2023 AW058).

Statistical analysis

R 4.2.1 was utilized for data assessment, with a p value < 0.05 deemed statistically significant. For the comparison of continuous variables, t-test, and Wilcoxon test were employed, while categorical variables were examined through chi-square test.

Results

Single-cell data processing and visualization

Quality control of scRNA data analysis was conducted through the"Seurat"package (Fig. 1A). Dimensionality reduction and visualization were performed using PCA and the UMAP methods (Fig. 1B and C). The batch correction was carried out using the"harmony"R package, with 20 PCs selected for clustering. The data quality control criteria were set as follows: 400 < nFeature_RNA

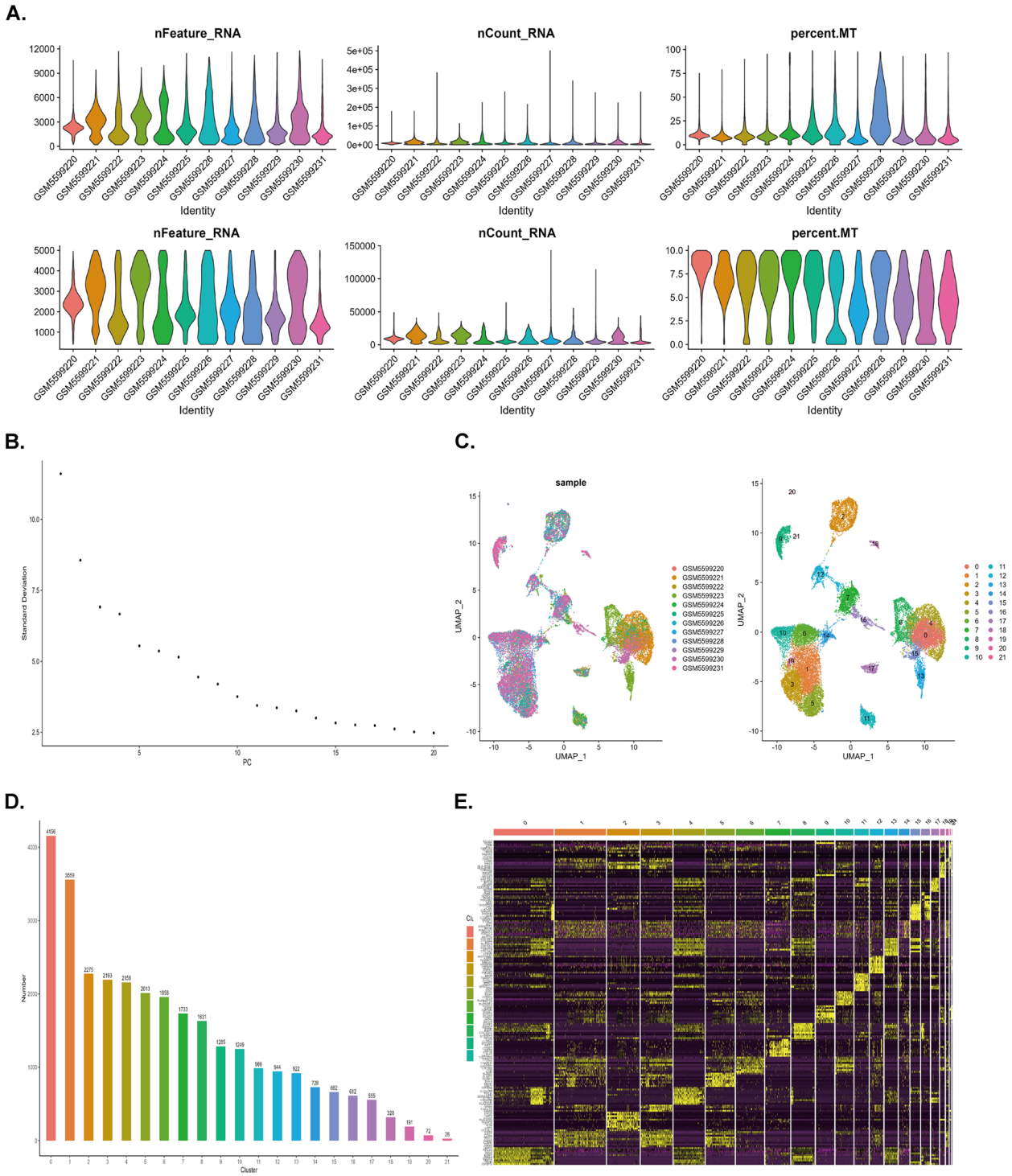

Fig. 1 Analysis of single-cell RNA (scRNA) data of ovarian cancer (OC). **a** Quality control of scRNA data (n = 12; 5 normal samples and 7 tumor samples). **b** Principal component analysis (PCA) for dimensionality reduction. **c** Visual representation using the UMAP method. **d** Batch correction using the"harmony"R package. **e** Heatmap of highly expressed genes specific to each subpopulation

< 5000, and the percentage of mitochondrial genes (percent.mt) < 10%. A total of 22 cell types were identified in OC tissues and normal tissues (Fig. 1D and E).

Single-cell subpopulation annotation and selection of cell types with the highest AUCell scores for MRGs

Based on the reference data from the HumanPrimaryCellAtlasData database, the"singleR"package was utilized for cell annotation, resulting in the annotation of 8 cell types. Clusters 9, 18, and 21 were identified as B cells, cluster 11 as endothelial cells, cluster 7 as epithelial cells, clusters 2 and 20 as monocytes, cluster 5 as NK cells, clusters 0, 4, 8, 13, 15, and 17 as smooth muscle cells, clusters 1, 3, 6, 10, 12, 14, and 19 as T cells, and cluster 16 as tissue stem cells (Fig. 2A and B). Subsequently, gene sets related to choline metabolism, glycolysis metabolism, lipid metabolism, and sphingolipid metabolism were combined and de-duplicated, resulting in a set of MRGs. AUCell scores were then calculated for all cells. Relatively higher AUCell scores were noted in monocytes; thus reclustering analysis was executed specifically on monocytes (Fig. 2C and D).

Reclustering analysis and annotation of marker genes to determine monocyte subpopulations

By conducting reclustering analysis of monocytes, six monocyte subpopulations were identified. Based on previous literature, the monocytes were manually annotated based on the expression of marker genes (Fig. 3A, B, and C). The resulting data found that cluster 0 exhibited high expression of such genes as *C1QA*, *C1QB*, *C1QC*, *APOE*, *TERM2*, and *MS4 A4 A*, which was annotated as $C1QC^+$ tumor-associated macrophages (TAMs). Cluster 1 showed high expression of genes, including *S100 A9*, *S100 A8*, and *VCAN*, and was annotated as $FCN1^+$ resident tissue macrophages (RTMs). Cluster 2 exhibited high expression of the *SPP1* gene and was annotated as $SPP1^+$ TAMs. Cluster 4 showed high expression of genes such as *MKI67*, *BIRC5*, *STMN1*, and *CDC20*, and was annotated as $MKI67^+$ TAMs. On the other hand, cluster 3 and cluster 5 did not exhibit distinctive expression patterns and were annotated as undefined monocytes (Fig. 3D and E).

Identification of marker genes for monocyte subpopulations based on MRG scoring

To evaluate gene scores in macrophages, the "AddModuleScore" function within the "Seurat" framework was employed. This assessment encompassed four distinct gene sets": choline metabolism, carbohydrate metabolism, lipid metabolism, and sphingolipid metabolism. Subsequently, radar plots were generated to examine the outcome (Fig. 4A, B, C, D, and E). It was found that these four gene sets had the highest scores in the $C1QC^+$ TAMs (Fig. 4B) and $FCN1^+$ RTMs (Fig. 4C) subpopulations (with the choline metabolism gene set showing the highest score). Therefore, marker genes were extracted from these two subpopulations for subsequent bulk RNA-seq analysis.

Differential expression analysis of marker genes in $C1QC^+$ TAM and $FCN1^+$ RTM subpopulations

Marker genes were extracted from the $C1QC^+$ TAM and $FCN1^+$ RTM subpopulations, and those with an average $\log_2$FC (avg_$\log_2$FC) > 0.5 were selected as marker genes. These marker genes were then combined with the previously mentioned four gene sets, resulting in a total of 1,308 genes for differential analysis.

Based on the comparison between tumor and normal samples, differential expression analysis was performed on the aforementioned genes. A threshold of FDR (adjusted p value) < 0.05 and $|\log_2 FC| > 0.58$ ($\log_2 1.5$) was utilized to screen for any gene displaying a substantial differential expression. The intersection of these genes with the previously selected marker genes resulted in a final set of 870 DEGs (Fig. 5A). The top 25 upregulated and downregulated DEGs based on FC were selected and visualized in a heatmap (Fig. 5B).

STRING database (https://cn.string-db.org/) was utilized to construct a PPI network of the DEGs. The DEGs from the combined gene set were imported into STRING, and a threshold of combined_score > 0.95 was used to screen for significant interactions. This method resulted in a PPI network with 347 nodes and 744 edges (Fig. 5C).

Construction and validation of a prognostic model based on MRG

In training set samples, univariate Cox regression analysis was executed based on the DEGs obtained earlier, along with clinical survival prognosis information. This analysis aimed to identify genes that were notably linked with overall survival prognosis. A threshold of p value less than 0.05 was set to screen for genes that showed significant correlation with prognosis and identified 19 genes significantly associated with prognosis (Fig. 6A). Based on the genes determined with a strong correlation with the survival prognosis in the previous step, the survival prognosis information from the training set samples was further utilized. Combining this information with the expression values of the genes in each sample, the LASSO tenfold cross-validation analysis was utilized to further screen for a gene combination that was relevant to the prognosis. Through this analysis, 18 genes that were associated with survival prognosis were found (Fig. 6B and C).

Subsequently, the aforementioned 18 genes were subjected to stepwise multivariable Cox regression analysis to construct a prognostic risk model consisting of 12

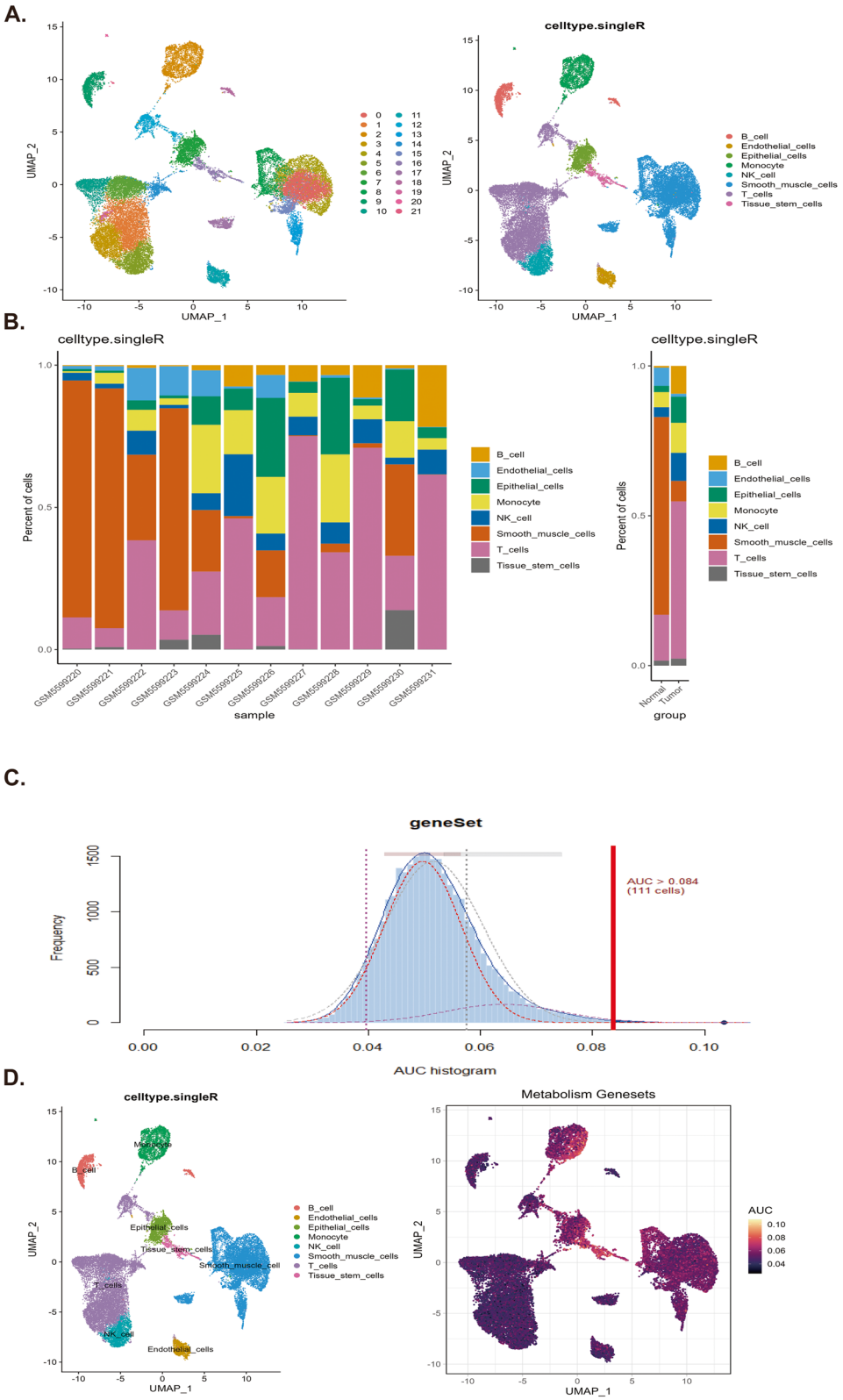

Fig. 2 Cell annotation and cell AUCell scores. **a** Uniform Manifold Approximation and Projection (UMAP) visualization of single-cell transcriptomes color-coded by annotated cell types. **b** Comparative analysis of cellular composition between normal (n = 5) and tumor (n = 7) specimens. **c** Histogram of AUCell scores. **d** Re-clustering analysis of monocytes

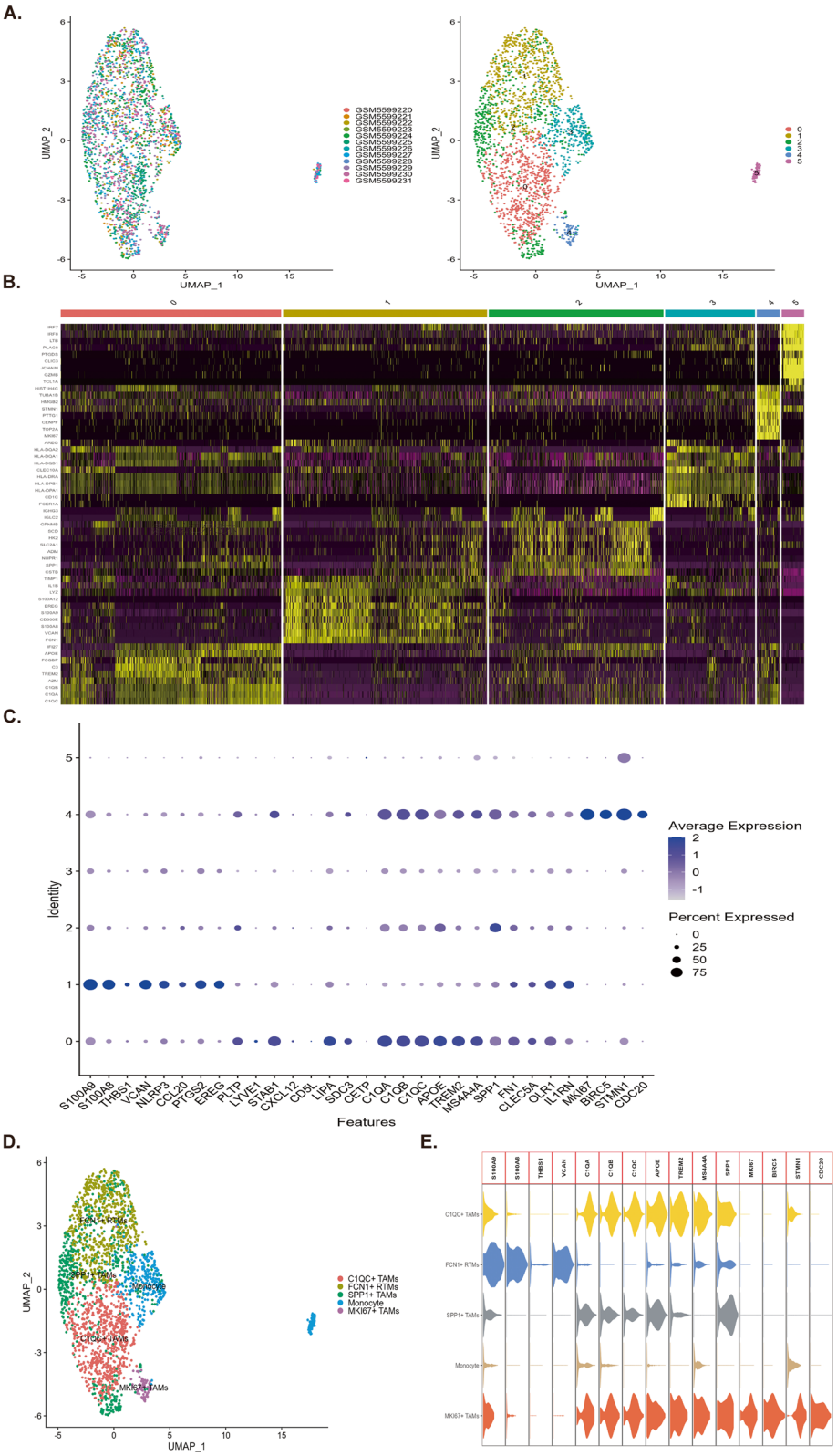

Fig. 3 Reclustering analysis and annotation of monocytes. **a** UMAP plot of cell atlas of monocytes. **b** Heatmap of top 10 marker genes in monocyte subpopulations. **c** Bubble plot depicting the expression of feature marker genes in monocyte subpopulations. **d** UMAP plot of monocyte subpopulations after annotation. **e** Violin plot showing the expression of marker genes in monocyte subpopulations

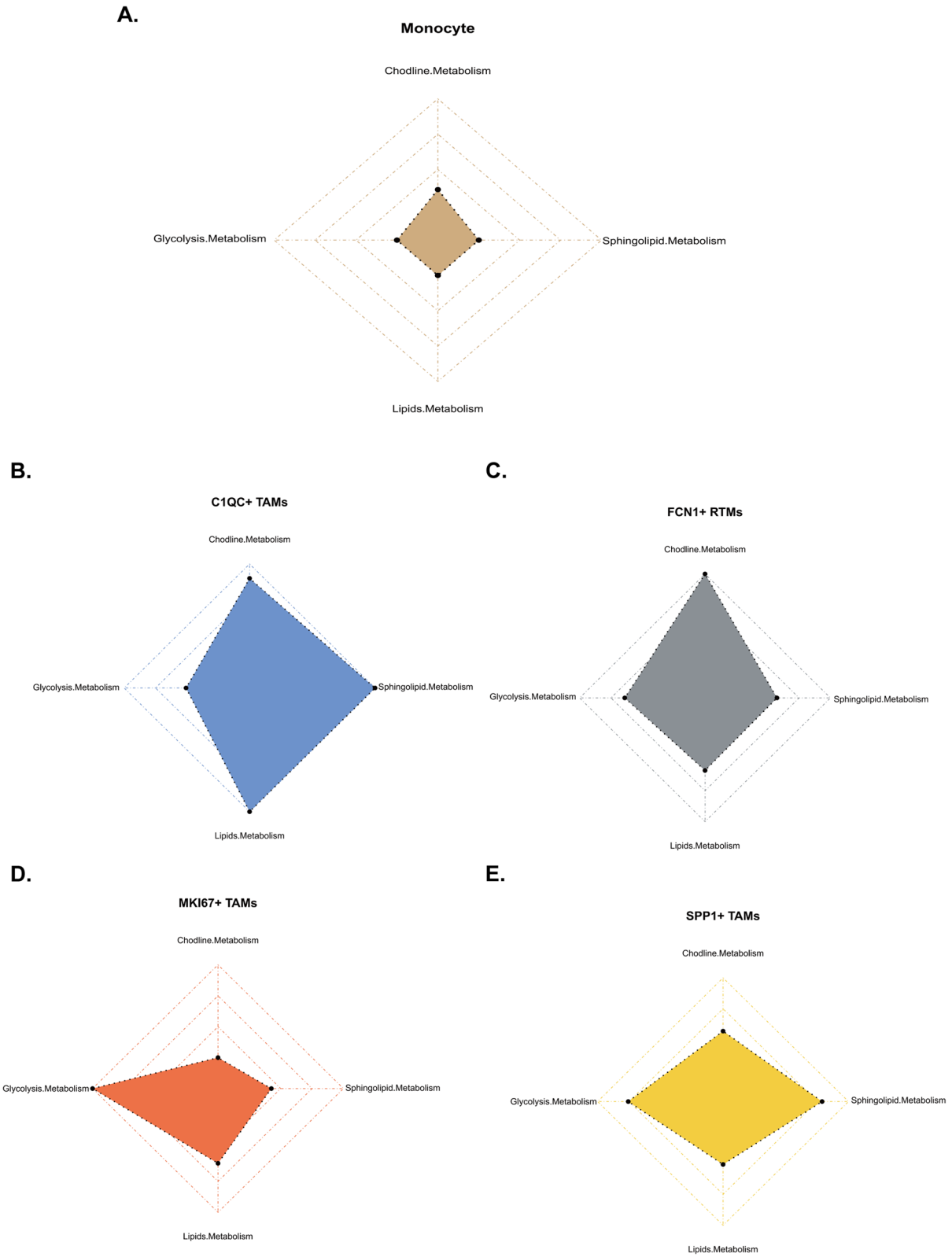

Fig. 4 Radar plots displaying gene scores for four metabolic pathways (glycolysis, lipid, choline and sphingolipid metabolism) across distinct monocyte subpopulations. **a** Radar plot of gene scores for all monocyte subpopulations. **b** Radar plot of gene scores for C1QC + tumor-associated macrophage (TAM) subpopulation. **c** Radar plot of gene scores for FCN1 + resident tissue macrophage (RTM) subpopulation. **d** Radar plot of gene scores for MKI67 + TAM subpopulation. **e** Radar plot of gene scores for SPP1 + TAM subpopulation

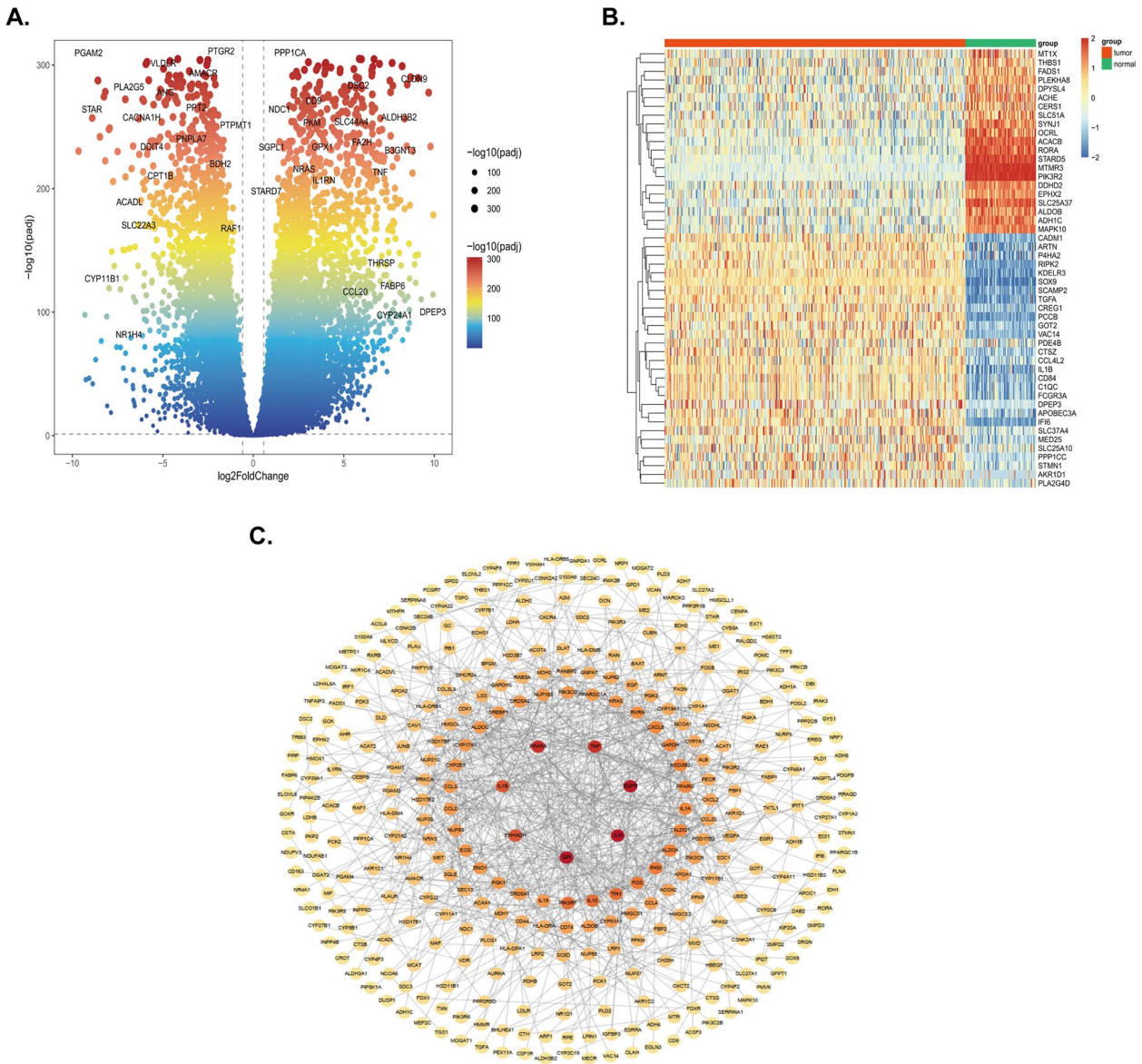

Fig. 5 Differential expression and functional network analysis of marker genes in C1QC + TAM and FCN1 + RTM subpopulations. **a** Volcano plot of differentially expressed genes (DEGs). **b** Heatmap of DEGs. **c** Protein–protein interaction (PPI) network of DEGs

(See figure on next page.)

Fig. 6 Construction and validation of the prognosis model for MRGs. **a** Forest plot of univariate Cox for DEGs. **b** and **c**: Distribution of LASSO coefficients for the selection of prognostic-related genes. **d** Kaplan–Meier (KM) curves associated with the RiskScore predictive model in the TCGA training set. Distribution of RiskScore (upper panel), survival time (middle panel), and expression heatmap (lower panel) in the TCGA training set. **e**: KM curves associated with the RiskScore predictive model in the TCGA testing set. Distribution of RiskScore (upper panel), survival time status (middle panel), and expression heatmap (lower panel) in the TCGA testing set. **f** KM curves associated with the RiskScore predictive model in the ICGC external validation set. Distribution of RiskScore (upper panel), survival time (middle panel), and expression heatmap (lower panel) in the ICGC external validation set. **g** KM curves associated with prognosis in the TCGA training set. **h** KM curves associated with prognosis in the TCGA testing set. **I** KM curves associated with prognosis in the ICGC external validation set. **j** ROC curves for 1-, 3-, and 5-year survival in the TCGA training set. **k** ROC curves for 1-, 3-, and 5-year survival in the TCGA testing set. **l** ROC curves for 1-, 3-, and 5-year survival in the ICGC external validation set

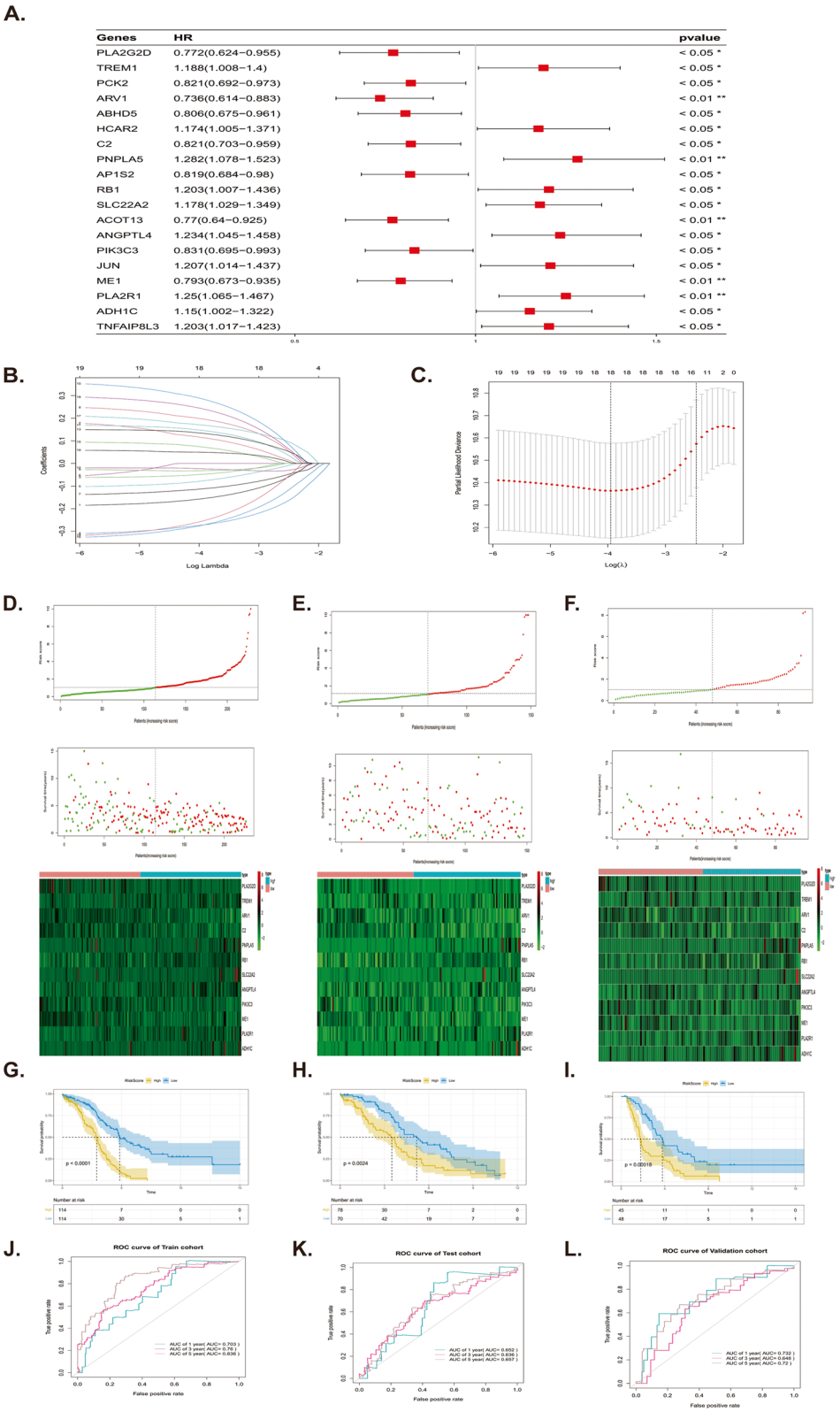

Fig. 6 (See legend on previous page.)

genes. The calculation formula of the RiskScore is as follows: RiskScore =PLA2G2D*(−0.209571108693993) + TREM1*0.152412209364298 + ARV1*(−0.348879506961556) + C2*(−0.158025519361435) +PNPLA5*0.227557191045807 +RB1*0.389666702110792 +SLC22A2*0.163668016093365 +ANGPTL4*0.159674280529018 +PIK3C3*(−0.339372997610123) +ME1*(−0.36406450675628) +PLA2R1*0.249748444269229 +ADH1C*0.276008705607345. Based on the median RiskScore, the samples of the TCGA training set were categorized into High_Risk (RiskScore >median RiskScore) and Low_Risk (RiskScore ≤median RiskScore) (Fig. 6D, E and F). The correlation between the grouping of High_Risk and Low_Risk based on the KM curves and actual survival prognosis information was evaluated, and ROC curves for 1-, 3-, and 5-year survival were plotted to calculate the corresponding AUC values. Moreover, the KM curves were plotted to comparatively assess the variance in prognosis between the two groups of patients. The results demonstrated a notable variance between High_Risk and Low_Risk groups, with poorer prognosis in the High_Risk group (p value <0.05). Additionally, the AUC values were calculated using the ROC curves for 1-, 3-, and 5-year survival, which were found to be 0.703, 0.76, and 0.836, respectively (Fig. 6G and J). Furthermore, to validate the accuracy of the model, the TCGA test dataset and the ICGC external validation dataset were used to verify and evaluate the model. The RiskScore calculation formula was applied to calculate the risk scores for both the test and external validation datasets. Based on the median RiskScore, the samples from both datasets were categorized into High_Risk and Low_Risk groups. KM curve analysis demonstrated notable prognostic variance between High_Risk and Low_Risk groups in both datasets (p value <0.05), with poorer prognosis observed in the High_Risk group (Fig. 6H and I). Additionally, ROC curves were used to calculate the AUC values for 1-, 3-, and 5-year survival. The AUC values for 1-, 3-, and 5-year survival in the TCGA test dataset were 0.652, 0.636, and 0.657, respectively. In the ICGC external validation dataset, the respective AUC values for 1, 3, and 5-year survival were 0.732, 0.648, and 0.72 (Fig. 6K and L).

Construction of nomogram for MRGs in OC

Through univariate Cox analysis for RiskScore and clinical factors (age, stage, and grade), it was found that some clinical features, including age, stage, and RiskScore, were significantly linked with prognosis (p value <0.001) (Fig. 7A). These factors underwent further analysis through multivariate Cox regression, resulting in the construction of a clinical risk model nomogram composed of age, stage, and RiskScore (p value <0.001). The model demonstrated a C-index of 0.669 (Fig. 7B). Using the nomogram, the clinical risk score, nomoScore, was calculated for TCGA-OC tumor samples (Fig. 7C). Based on the median nomoScore, all samples were divided into High_nomoRisk and Low_nomoRisk groups. KM curves were utilized to compare the survival differences between the two groups of patients (Fig. 7D; p value <0.001), revealing a poorer prognosis in the High_nomoRisk group. ROC curves were utilized to calculate the respective AUC values for 1-, 3-, and 5-year survival, which were found to be 0.763, 0.715, and 0.657 (Fig. 7E). Subsequently, the clinical risk model was evaluated using calibration curves (Fig. 7F) and DCA, with the data demonstrating a favorable predictive performance of the model (Fig. 7G).

Functional analysis and pan-cancer analysis of MRG-based prognostic model

The GeneMANIA database (http://genemania.org/) was adopted to identify genes with similar functional characteristics to the model genes. This database facilitated the construction of co-expression networks and PPI networks. By leveraging this approach, their biological functions were projected and inferred. Notably, the genes *ADH1 C*, *PLA2R1*, *ARV1*, *CES1*, and *ACSL1* in the model gene set exhibited various metabolism-related biological functions (Fig. 8A and B). Based on the GSCALite database, pan-cancer analysis was conducted on the model gene set, revealing significant differences in mRNA expression, CNV, methylation, and SNV in multiple tumors (Fig. 8C, D, E, and F). Furthermore, the mutation frequency of the model gene set at the pan-cancer level was analyzed, and it was found that the *RB1* gene had the highest mutation frequency and occurred in multiple types of tumors (Fig. 8G).

Expression of MRG-based prognostic model gene set in scRNA and spatial transcriptomic data

Based on the scRNA expression profiles, the expression patterns of model genes were analyzed in different cell types (Fig. 9A). Using spatial transcriptomic data of OC, cells were grouped into 12 clusters with the expression of each gene assessed in each cluster (Fig. 9B and C).

Functional enrichment analysis and immune landscape visualization of DEGs in the MRG-based prognostic model in HRG

Differential analysis was conducted on genes in the HRG, and DEGs were selected using a threshold of FDR-corrected p value <0.05 and $|\log_2 FC|$> 1, resulting in 213 DEGs (Fig. 10A). The top 25 DEGs with the highest up- and down-regulation FCs were selected and plotted in a heatmap (Fig. 10B). Further assessment through GO

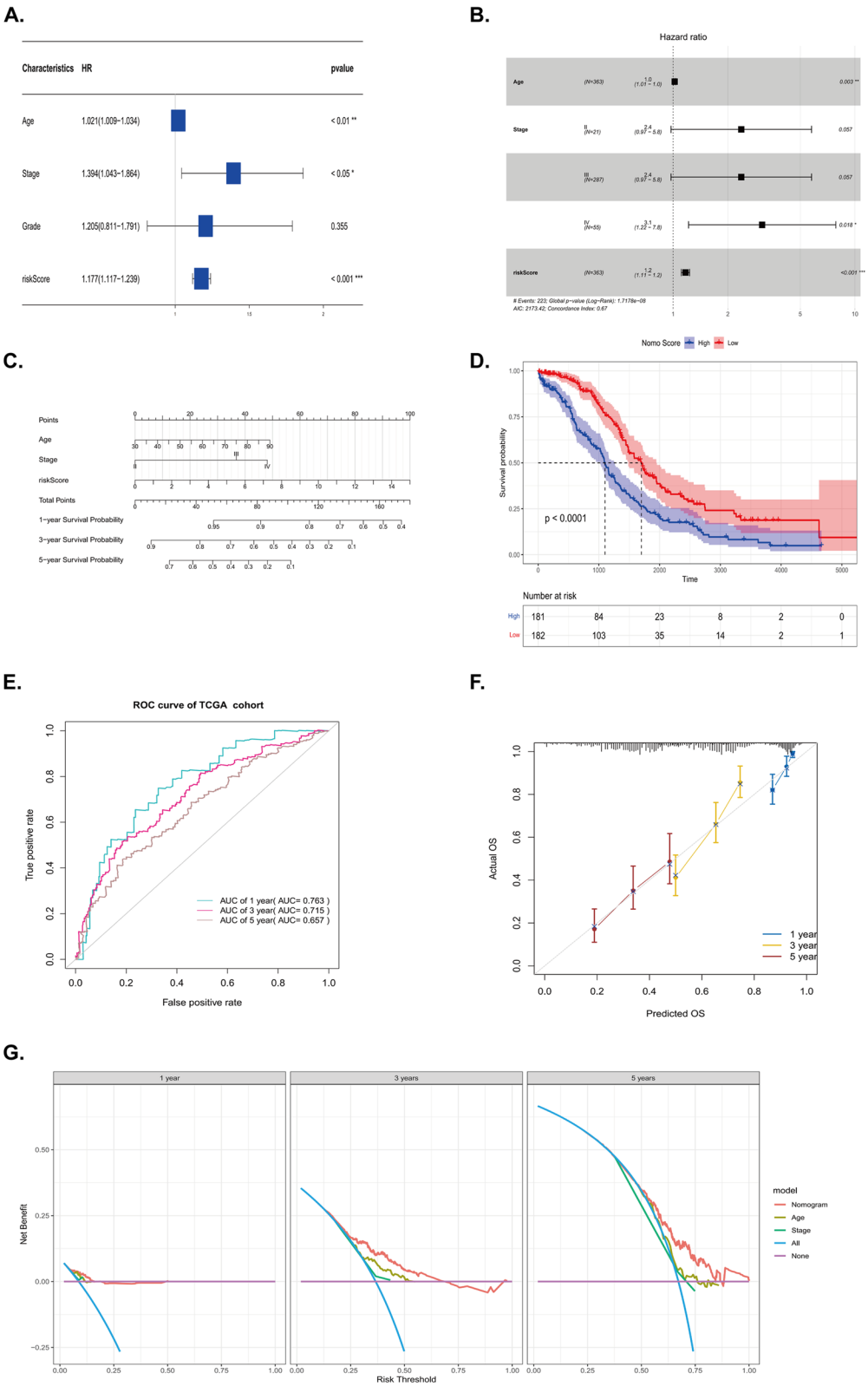

Fig. 7 Construction of nomogram for MRGs in patients with OC. **a** Forest plot of univariate Cox analysis for clinical factors and RiskScore. **b** Forest plot showing the multivariate Cox analysis of independent prognostic factors. **c** Nomogram depicting the clinical risk model. **d** Survival curves for the clinical risk model. **e** ROC curves for the clinical risk model. **f** Calibration curves for 1-, 3-, and 5-year survival in the clinical risk model. **g** Decision curve analysis (DCA) curves for 1-, 3-, and 5-year survival in the clinical risk model. * *p* value < 0.05; ** *p* value < 0.01; *** *p* value < 0.001

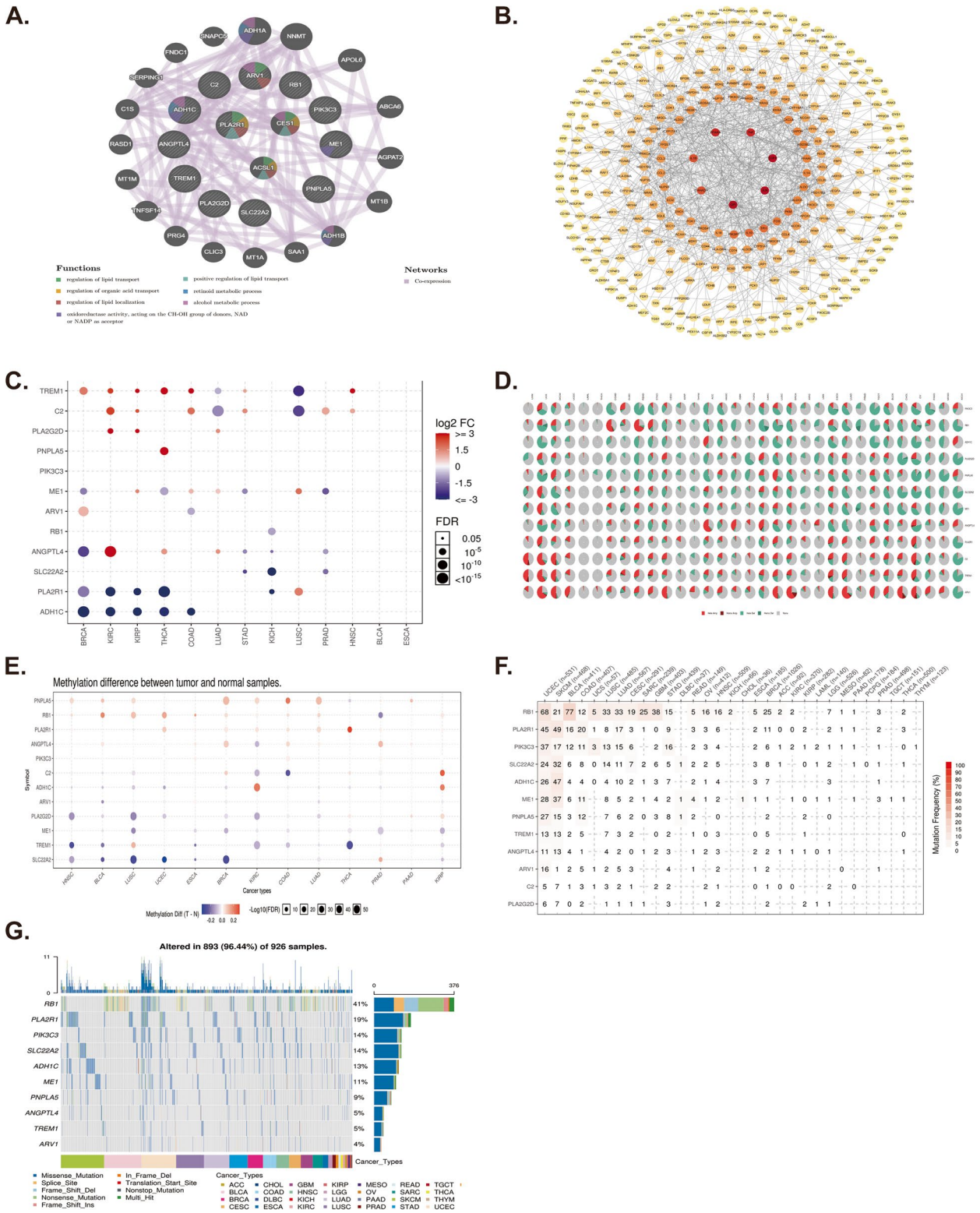

Fig. 8 Prediction of biological functional analysis using a prognostic model of the gene set and pan-cancer analysis. **a** Co-expression network of the prognostic model gene set generated by GeneMANIA. **b** PPI network of similar genes in the prognostic model gene set. **c** Differential expression of model genes in pan-cancer analysis. **d** Percentage distribution of copy number variation (CNV) of model genes in pan-cancer analysis. **e** Differential methylation of model genes. **f** Percentage distribution of single nucleotide variation (SNV) of model genes in pan-cancer analysis. **g** Waterfall plot of mutations of model genes in pan-cancer analysis

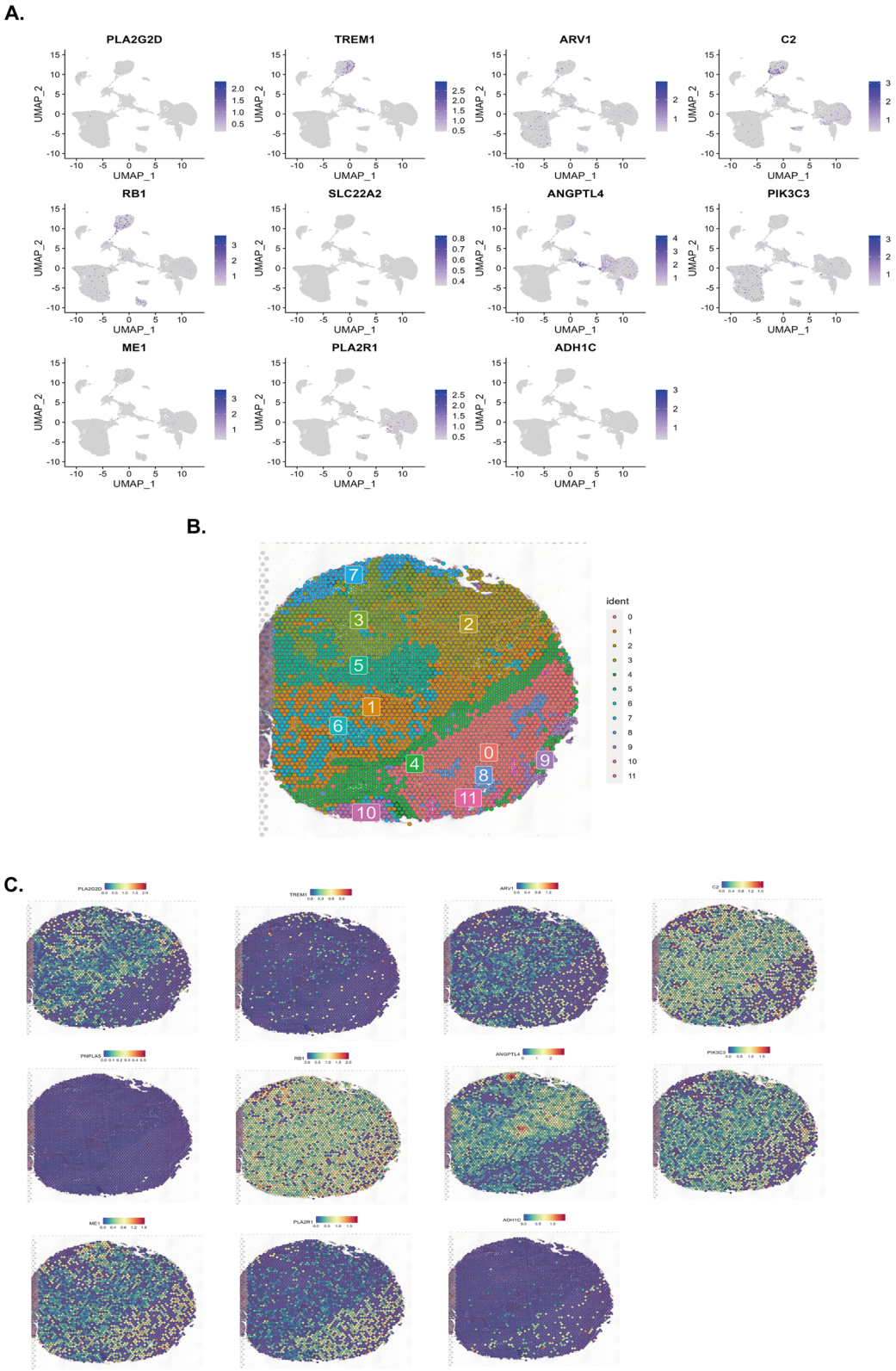

Fig. 9 Expression patterns of gene set in the MRG-based prognostic model in scRNA and spatial transcriptomic data. **a** Expression of model genes in scRNA data of OC. **b** Cell subpopulations in spatial transcriptomic data of OC. **c** Expression of model genes in cell subpopulations of spatial transcriptomic data of OC

enrichment analysis revealed significant enrichment in 74 biological process (BP) pathways, 1 cellular component (CC) pathway, and 23 molecular function (MF) pathways. The data indicated that the top 5 significantly enriched pathways were"ureteric bud development, mesonephric epithelium development, mesonephric tubule development, mesonephros development, and nephron tubule morphogenesis"(Fig. 10C). KEGG enrichment analysis identified 3 significantly enriched pathways:"neuroactive ligand-receptor interaction, IL-17 signaling pathway, and Cytokine-cytokine receptor interaction"(Fig. 10D). Based on the CIBERSORT and the EESTIMATE algorithms, IME analysis of HRG and LRGs was conducted. It was found that 7 types of immune cells, namely"macrophages M1, monocytes, T cells gamma delta, T cells follicular helper, T cells CD4 memory activated, T cells CD8, and plasma cells,"as well as ImmuneScore, exhibited significant differences between the HRG and LRG (Fig. 10E and F). The anti-cancer immune response activity score of patients with OC between the HRG and LRG was assessed using the TIP database. It was demonstrated that the anti-cancer immune activity in the LRG was considerably elevated in comparison to that in the HRG (Fig. 10G). The ssGSEA score algorithm was used to analyze the recruitment of various immune cells and visualize the results in a heatmap (Fig. 10H). The expression variance of ICGs was assessed across the HRG and LRG, and the acquired data revealed that multiple ICGs exhibit differential expression (Fig. 10I). Based on the TIDE database analysis to predict the benefit of ICI therapy in patients with OC, the differences in TIDE scores were comparatively assessed between the HRG and LRG. Significantly different Exclusion scores were observed between patients in the HRG and LRG (Fig. 10J).

Somatic mutation analysis results

Based on the OC-related somatic mutation data from TCGA, the top 20 genes with the highest mutation frequencies were compared in the HRG and LRG. The acquired data indicated that *TP53*, *TTN*, *CSMD3*, and *MUC16* demonstrated higher mutation frequencies in the LRG (Fig. 11A). Whereas, in the HRG, *TP53*, *TTN*, *FAT3*, and *CSMD3* had higher mutation frequencies (Fig. 11B). The co-mutation correlations among the top 20 genes were investigated as well. In the LRG, significant co-mutation correlations were observed between *DST* and *CSMD3* (p value < 0.01), *ASPM* and *MUC17* (p value < 0.01), *SYNE2* and *TP53* (p value < 0.01), *RYR2* and *MUC17* (p value < 0.01), and *MACF1* and *CSMD3* (p value < 0.01) (Fig. 11C). In the HRG, *AHNAK* and *TTM* showed a significant co-mutation correlation (p value < 0.01) (Fig. 11D).

Small molecule drugs predicted using the CMap tool for OC treatment and molecular docking with target proteins

A total of 132 upregulated genes and 81 gene data in the HRG and LRG were used to predict small molecule drugs for the treatment of OC in the CMap database. The top 5 genes with the highest FCs were selected as target genes (*CNGA2*, *ANHX*, *CHIA*, *AGTR2*, and *LY6D*). Using these five genes as targets, a screening process was executed in the CMap database, excluding drugs without pertinent information on small molecule drugs. This process culminated in the final selection of only two genes as potential targets for small-molecule drugs. However, one of these genes, *CHIA*, had a molecular weight beyond the scope of being docked in AutoDock. Ultimately, two drugs, PD-123319, and candesartan Cilextil, were selected for their potential targeting of the *AGTR2* gene. The 3D structures of two small molecule drugs were downloaded from PubChem platform, and protein annotation information for the *AGTR2* gene was obtained from the Uniprot database. The protein structure of this gene was downloaded from the PDB database. The Pymol method was used to remove water molecules and small molecule ligands from the target protein and small molecule drugs. The AutoDock was utilized to perform molecular docking based on the Generic algorithm. The docking energy between the AGTR2 protein and PD-123319 molecule was −4.39 kcal/mol (Fig. 12A), while the docking energy between the AGTR2 protein and candesartan Cilextil molecule was −4.64 kcal/mol (Fig. 12B).

(See figure on next page.)

Fig. 10 Functional enrichment analysis and immune landscape visualization of DEGs in the high-risk group (HRG) and low-risk group (LRG). **a** Volcano plot of DEGs in the MRG-based prognostic model between HRG and LRG. **b** Heatmap of DEGs between HRG and LRG. **c** Gene Ontology (GO) enrichment analysis of DEGs in the HRG and LRG. **d** Kyoto Encyclopedia of Genes and Genomes (KEGG) enrichment analysis of DEGs in the HRG and LRG. **e** CIBERSORT calculation of the relative abundance of immune cell types in the samples of HRG and LRG. **f** ESTIMATE calculation of ImmuneScore and StromalScore in the samples of HRG and LRG. **g** Violin plot showing overall activity differences of TIP database analysis in the HRG and LRG. **h** Heatmap of ssGSEA scores between HRG and LRG. **i** CIBERSORT calculation of the relative abundance of ICGs in the samples of HRG and LRG. **j** Differences in Exclusion scores between patients between HRG and LRG. * p value < 0.05; ** p value < 0.01; *** p value < 0.001

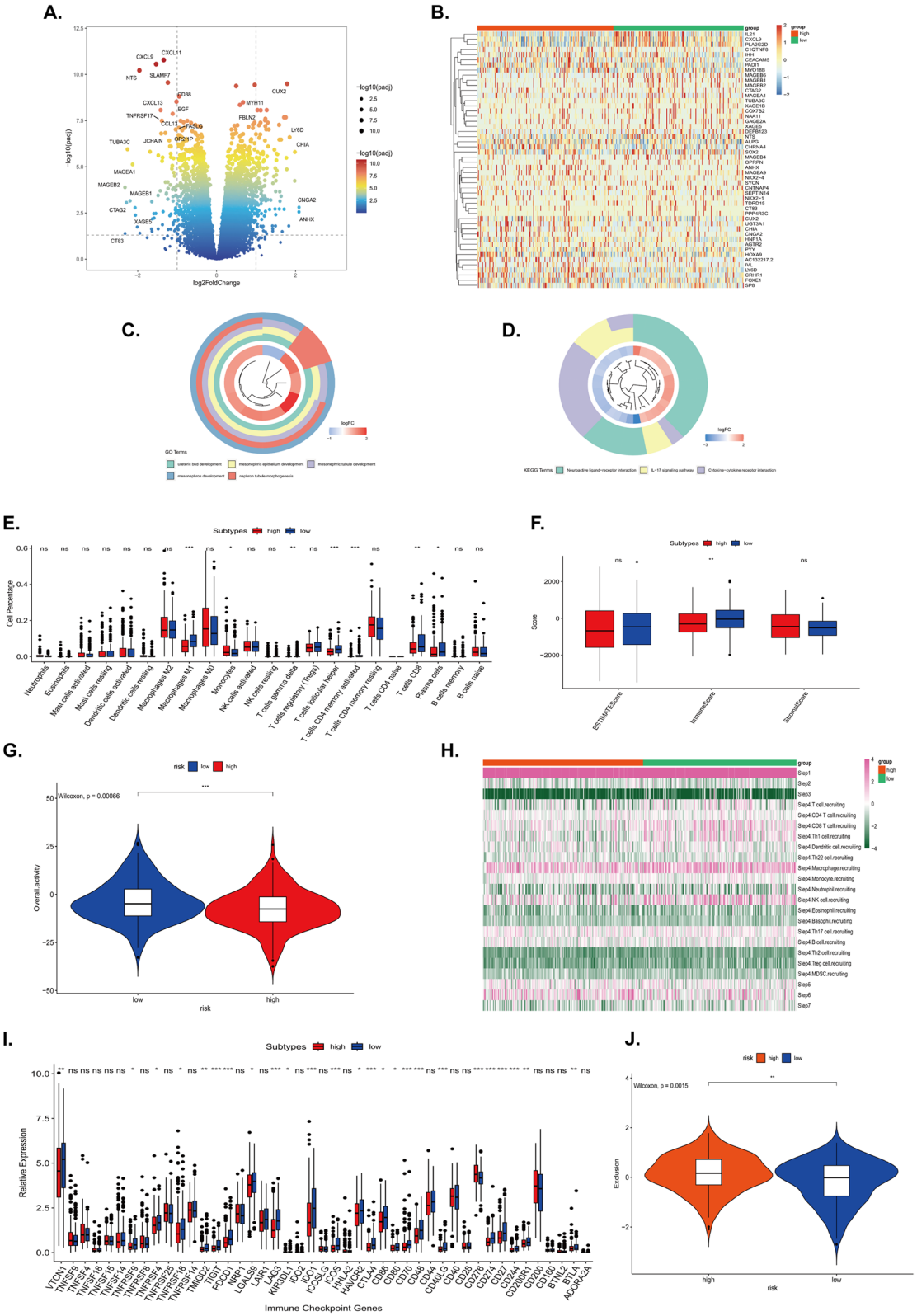

Fig. 10 (See legend on previous page.)

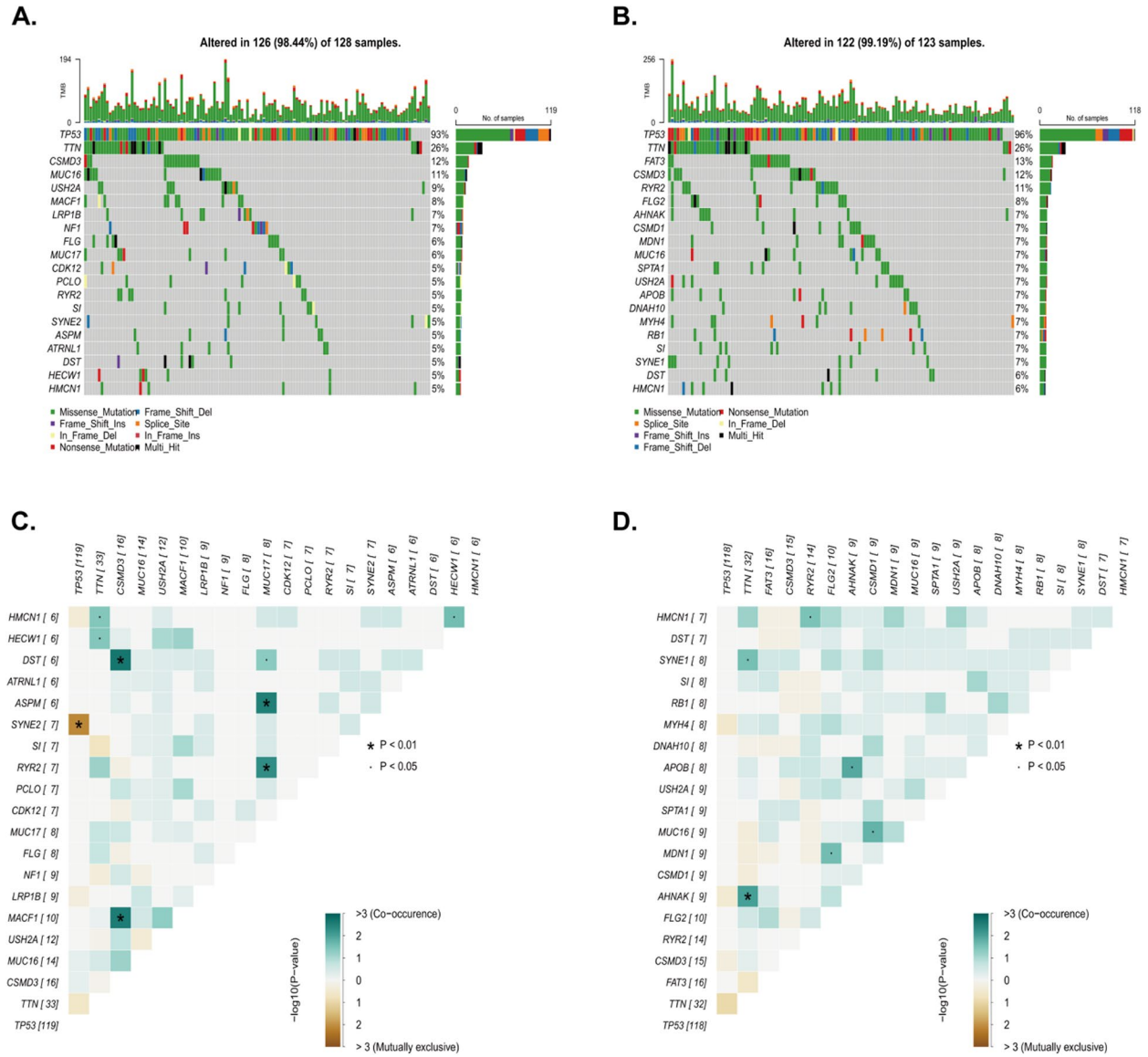

Fig. 11 Somatic mutation and co-mutation analysis in the HRG and LRG. **a** Waterfall plot of somatic mutations in the HRG. **b** Waterfall plot of somatic mutations in the LRG. **c** Heatmap showing co-mutation correlations in the HRG. **d** Heatmap showing co-mutation correlations in the LRG. * *p* value < 0.05; ** *p* value < 0.01

In vivo and in vitro experiments validating the prognostic significance of TREM1 as an MRG

This research further assessed the prognostic ability of *TREM*1, a prognostically significant gene related to metabolism, in OC using a metabolism-related prognostic model [21, 22]. Immunohistochemical staining of tissue microarrays revealed significantly elevated expression of the TREM1 in tumors. Semi-quantitative analysis of TREM1 expression by immunohistochemical staining was performed, and the TREM1 positive rate was noted to be considerably lower in normal ovarian tissues compared to OC tissues (Fig. 13A and B). Furthermore, the expression levels of *TREM1* in various tumor cell lines were determined using RT-qPCR. The research noted that considerably heightened expression levels of *TREM1* were observed in SKOV3 and ES-2 cell lines compared to normal ovarian epithelial cells (Fig. 13C). Hence, we conducted further verification using SKOV3 and ES-2 cell lines. The constructed shRNA plasmids of sh-TREM1#1 and sh-TREM1#2 notably knocked down the TREM1 expression in SKOV3 and ES-2 cell lines (Fig. 13D and E). CCK-8 assay revealed that both sh-TREM1#1 and sh-TREM1#2

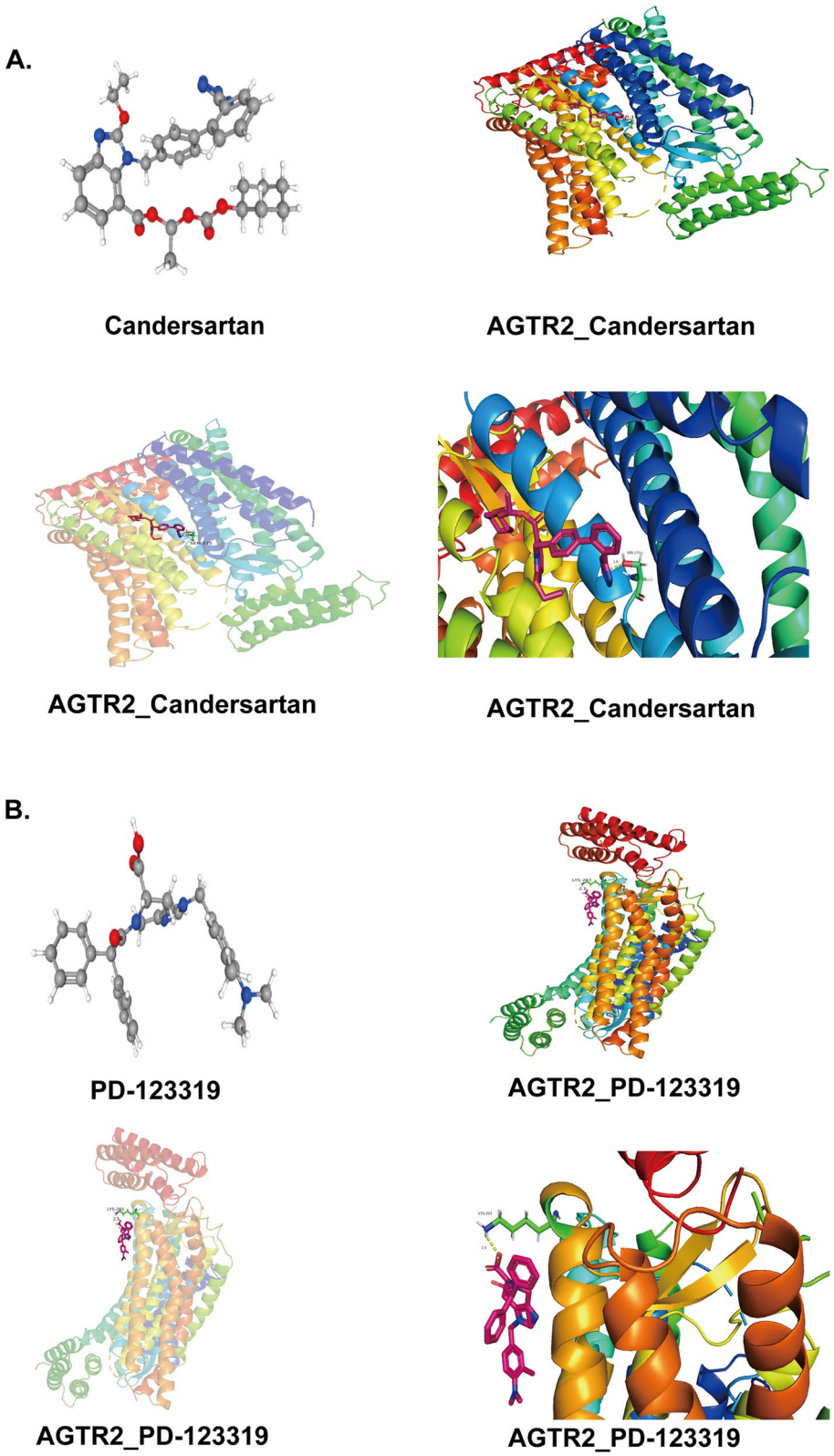

Fig. 12 Molecular docking of therapeutic drugs against OC. **a** 3D structure of the drug molecule of PD-123319 and its docking state with AGTR2 protein. **b** 3D structure of the candesartan Cilextil drug molecule and its docking state with AGTR2 protein

considerably diminished the proliferation ability of SKOV3 and ES-2 cells (Fig. 13F and G. Transwell experiments also demonstrated that both sh-TREM1#1 and sh-TREM1#2 decreased the migration ability of SKOV3 (Fig. 13H and I) and ES-2 (Fig. 13J and K) cells. Furthermore, a stable shTREM1-transfected cell line was generated, and it was observed that the knockdown of TREM1 repressed tumor growth in mice (Fig. 13L), with significantly lowered tumor volume (Fig. 13M) and weight (Fig. 13N) in the sh-TREM1 group compared to the wild-type group.

Discussion

OC, as one of the most important gynecological tumors, has the highest mortality rate among gynecological tumors. Over 3 million women are diagnosed with OC every year, and 152,000 women die from it, posing a serious threat to the health of women [23]. Early-stage OC lacks noticeable signs and symptoms and progresses rapidly from early to advanced stages [24]. Therefore, it is crucial to develop effective prognostic biomarkers and explore new therapeutic drugs and targets for the treatment of OC.

Normal cells require energy for growth, division, and survival [11]. Compared to normal cells, tumor cells demonstrate unique metabolic phenotypes. Tumor cells often maintain proliferation by altering their metabolism, characterized by changes in nutrient metabolism, rapid biomass production, and the management of redox balance [25, 26]. Carbohydrate metabolism, lipid metabolism, choline metabolism, and sphingolipid metabolism are strongly linked with the progression of OC. Previous studies have found that enhanced glycolysis and glucose uptake are metabolic features of OC [27]. Changes in lipid metabolism are closely associated with the proliferative and metastatic capacity of OC cells, as rapidly proliferating cancer cells increase their demand for fatty acids for cell membrane construction, formation of signaling molecules, and energy support [11, 27]. Choline metabolism, a newly discovered abnormal tumor metabolism, is a novel metabolic marker characterized by increased phosphocholine (PCho) and total choline-containing compounds (tChos). Granata et al. have found that the downregulation of choline kinase alpha (ChoK-α) curtails the invasiveness of OC cells and confers sensitivity to chemotherapeutic drugs [28, 29]. Sphingolipid metabolism has also been identified as a key factor in the progression and drug resistance of OC, with sphingolipids and enzymes in the sphingosine-1-phosphate pathway critically implicated in influencing OC development and resistance to chemotherapy [30].

Beyond basic research, therapeutic strategies and diagnostic techniques focusing on metabolic pathways have garnered significant attention in clinical research over recent years. Despite this, their translation into clinical practice remains fraught with numerous challenges. This discussion examines the potential and constraints of interventions targeting the four principal metabolic pathways, informed by recent clinical studies. The Warburg effect, also known as aerobic glycolysis, is a significant hallmark of tumor cell metabolism [31, 32]. Preclinical studies have demonstrated that inhibition of these key glycolytic enzymes can markedly reduce tumor growth. For instance, inhibitors targeting PKM2 and LDHA have shown potential in effectively suppressing tumor growth across various tumor models. These findings provide a crucial theoretical foundation and practical evidence for the development of novel anticancer therapeutic strategies [33, 34]. Targeting the glycolytic pathway may not only inhibit the proliferation of tumor cells but also alter their metabolic milieu, thereby enhancing the efficacy of conventional treatment modalities. Lipid metabolism reprogramming plays a crucial role in cancer cells, particularly in the processes of fatty acid synthesis and oxidation. Fatty acid synthase (FASN) and carnitine palmitoyltransferase 1 (CPT1 A) are two key enzymes that exert a dual role in regulating lipid metabolism. Overexpression of FASN has been observed in breast cancer patients and has been demonstrated for its role in cancer

(See figure on next page.)

Fig. 13 In vivo and in vitro experimental validation of the metabolism-related prognostic gene TREM1. **a** Immunohistochemical staining of the TREM1 expression; **b** Semi-quantitative analysis by immunohistochemistry to compare the proportion of TREM1-positive cells in normal ovarian tissue (n = 45) versus OC tissue (n = 45); **c** RT-qPCR detection of gene expression levels of TREM1 in normal ovarian epithelial cell line IOSE-80 and OC cell lines SKOV3, ES-2, and CAOV3; **d** RT-qPCR validation of the efficiency of TREM1 knockdown by shRNA in SKOV3 cell line; WT (wild-type, untransfected cells); sh-NC (cells transfected with a non-coding scrambled shRNA control) (**e**) RT-qPCR validation of the efficiency of TREM1 knockdown by shRNA in ES-2 cell line; **f** CCK8 assay to measure the effect of TREM1 knockdown by shRNA on the proliferation ability of SKOV3 cells; **g** CCK8 assay to measure the effect of TREM1 knockdown by shRNA on the proliferation ability of ES-2 cells; **h** Transwell assay to measure the effect of TREM1 knockdown by shRNA on the migration ability of SKOV3 cell line; **i** Statistical analysis of migrated cell numbers in SKOV3 cell line; **j** Transwell assay to measure the effect of TREM1 knockdown by shRNA on the migration ability of ES-2 cell line; **k** Statistical analysis of migrated cell numbers in ES-2 cell line; **l** Tumor formation assay in BALB/c-nu/nu mice to evaluate the tumorigenic ability of stably transfected SKOV3 cell line with reduced TREM1 expression (WT: n = 4; sh TREM1:n = 4); **m** Tumor volume in mouse xenograft model; **n** Tumor weight in mouse xenograft model; *$p < 0.05$; **$p < 0.01$, ***$p < 0.001$, ****$p < 0.0001$

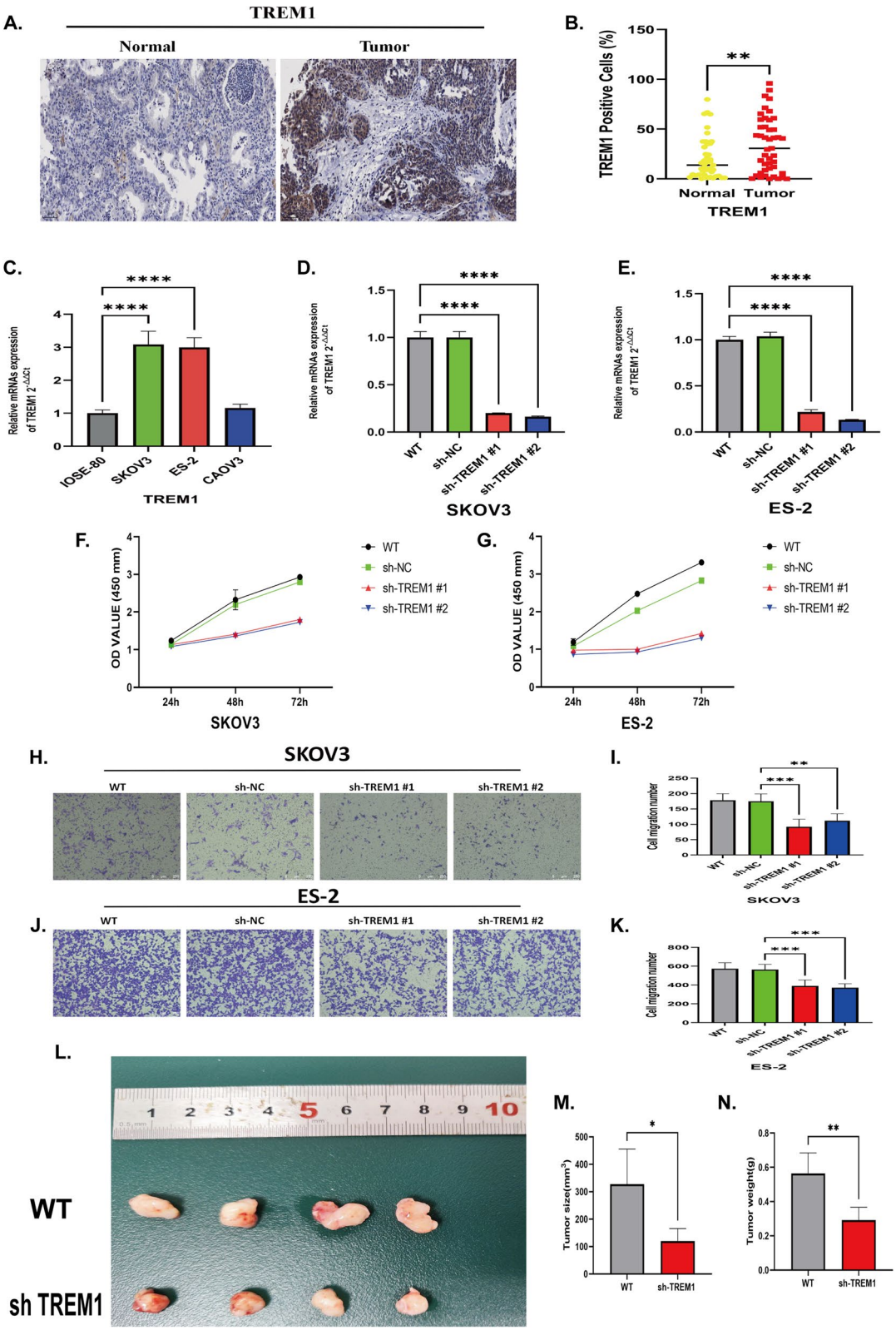

Fig. 13 (See legend on previous page.)

[35]. Moreover, CPT1 A plays a significant role in fatty acid oxidation by facilitating the entry of fatty acids into the mitochondria for β-oxidation, which is particularly important for tumor cells under hypoxic conditions [36]. For instance, study has found that the combination of FASN inhibitors with bevacizumab shows good tolerability and therapeutic signals in recurrent high-grade astrocytomas [37]. Therefore, future research may further explore the combination of FASN inhibitors with other targeted therapies or immunotherapies. Choline metabolic imaging, particularly choline Positron Emission Tomography/Computed Tomography (PET/CT), plays a pivotal role in the diagnosis and management of prostate cancer. Studies have demonstrated that choline PET/CT exhibits high sensitivity and specificity in both staging prostate cancer and detecting disease recurrence [38]. Furthermore, choline PET/CT demonstrates superior accuracy in detecting lymph node metastases and distant lesions, establishing it as the imaging modality of choice for patients with biochemical recurrence [38]. In neuro-oncology, choline PET/CT has shown exceptional diagnostic utility. Research indicates that radiolabeled choline PET or PET/CT achieves high diagnostic accuracy in differentiating high-grade from low-grade gliomas, as well as distinguishing malignant from benign intracranial lesions [39]. Compared to conventional 18 F-fluorodeoxyglucose (FDG) PET, choline PET exhibits enhanced sensitivity and specificity in detecting tumor recurrence and guiding stereotactic biopsy site selection in cerebral neoplasms [39]. Therapeutic developments targeting choline kinase alpha (CHKα) have encountered clinical challenges. Although the CHKα inhibitor TCD-717 demonstrated potent antitumor activity in a phase I clinical trial, the study was halted due to dose-limiting toxicities [40]. These findings underscore the necessity for developing more selective allosteric inhibitors to improve therapeutic safety and efficacy. Notably, emerging evidence highlights crosstalk between choline metabolism and epigenetic regulation mechanisms, such as histone acetylation. This interaction may present novel opportunities for therapeutic synergy through combination therapies with epigenetic-modulating agents [38, 41].

As the research on tumor metabolism deepens, our understanding of the metabolic alterations occurring after tumor formation is becoming increasingly profound. The influence of metabolism on tumor initiation and development is not solely determined by one specific metabolic change; instead, the combined effect of multiple metabolic alterations collectively impacts tumor proliferation and metastasis. Therefore, in this study, scRNA data from 5 normal ovarian samples and 7 OC samples was utilized. After processing and visualizing the scRNA data, the different cell subpopulations in OC were annotated and the highest-scoring monocytes were selected based on AUCell scores for MRGs. Subsequently, the monocytes were classified into subgroups with subsequent analysis of the gene scores of choline metabolism, carbohydrate metabolism, lipid metabolism, and sphingolipid metabolism in macrophages. The data indicated the highest gene scores in two cell subpopulations, C1QC^{+} TAMs, and FCN1^{+} RTMs, and subsequent Bulk RNAseq analysis was performed using these two subgroups. Based on these marker genes, a prognostic model was established consisting of 12 MRGs, which demonstrated favorable prognostic performance. Furthermore, pan-cancer analysis and functional analysis were conducted using the gene set data from the prognostic model. The predicted results revealed multiple metabolic-related functions enriched in the model gene set, with widespread changes observed at the mRNA expression, CNV, DNA methylation, and SNV levels across various tumors. Patients with OC were categorized into HRG and LRG using the model gene set. In the context of the IME, significant differences were witnessed in various immune cells between the HRG and LRG. Furthermore, when assessing anti-cancer immune activity, we found that patients with OC in the LRG exhibited more favorable immune activity. Additionally, the prediction of outcomes for immunotherapy in patients with OC indicated that those in the LRG were less likely to experience metastasis.

We have further explored the small molecule drugs for patients with OC, as well as their corresponding target proteins. The predictive results suggested that the angiotensin II receptor antagonists candesartan and PD-123319 might be potential drugs for the treatment of OC. The potential targets of these two drugs in OC might be the *ATGR2* receptors. Angiotensin II receptor antagonists have been highlighted in multiple studies to confer anti-tumor capacity. Okazaki et al. have unveiled that candesartan can attenuate the proliferation and fibrosis of gastric cancer [42]. Tabatabai et al. have uncovered that candesartan can constrain the proliferative and fibrotic potential of colon cancer by thwarting the angiotensin II receptor by antagonists [43]. The process governing these effects of candesartan is likely linked to its capacity to diminish the expression of vascular endothelial growth factor (VEGF) and TGF-β1, induce changes reminiscent of epithelial-to-mesenchymal transition and modulate oxidative and antioxidant status [42–44]. In addition, enormous clinical trials have expounded that diminishing angiotensin II receptors by antagonists can have a positive impact on tumor treatment [45, 46]. However, currently, there is limited knowledge regarding the use of angiotensin II receptor antagonists in the research of OC. It is considered that candesartan and PD-123319,

among other angiotensin II receptor antagonists, may represent a novel research discovery and potential anticancer drugs in the treatment of OC.

Importantly, in vitro and in vivo experiments were carried out to validate the function of less-studied genes in the prognostic model gene set. The research found that downregulation of TREM1 expression can halt the proliferative and migratory ability of OC cells. Previous research has documented that overexpression of TREM1 is associated with an unsatisfactory prognosis and is closely related to immune infiltration and immune regulation in various tumors [21]. TREM1 may serve as an independent and effective prognostic biomarker for patients with OC. In recent years, research on the functions of TREM1 in disease microenvironments has transcended its traditional role in immune regulation, progressively unveiling its central position in the crosstalk between metabolic reprogramming and immune responses. Multidimensional evidence demonstrates that TREM1 shapes immune cell functionality by modulating key metabolic pathways, thereby influencing pathological progression in diverse diseases. In acute lung injury models, TREM1 drives macrophage glycolytic reprogramming via the PI3 K/AKT/mTOR-HIF-1α axis, directly promoting activation of the NLRP3 inflammasome/caspase-1 pathway [22]. Notably, mTOR inhibitors and HIF-1α antagonists concurrently suppress both metabolic remodeling and inflammatory activation, suggesting TREM1 may act as a molecular bridge linking cellular energy metabolism to innate immunity. This synergistic metabolic-inflammatory regulatory mechanism is likely operative across other inflammatory disorders. In metabolic disorder-related diseases, TREM1's regulatory network extends to lipid metabolism. Atherosclerosis studies reveal that TREM1 expression is markedly upregulated in circulating and plaque-infiltrating myeloid cells of Apoe-/- mice under dyslipidemic conditions [47]. Given the critical role of lipid metabolic dysregulation in tumor microenvironments, this finding implies TREM1 may participate in tumor immune evasion by modulating myeloid cell lipid metabolism, though precise mechanisms require further elucidation. Tumor microenvironment studies highlight TREM1's distinctive role in hypoxia-mediated immunometabolic remodeling. In hepatocellular carcinoma models, HIF-1α directly activates TREM1 expression in tumor-associated macrophages (TAMs), enhancing their immunosuppressive functions and inducing PD-L1-mediated therapeutic resistance [48]. While this study did not directly validate TREM1's impact on tumor metabolism, hypoxia—a primary driver of metabolic reprogramming such as the Warburg effect—suggests TREM1 may influence tumor progression through dual mechanisms: as a HIF-1α downstream effector regulating immune cell metabolic phenotypes, and indirectly by altering extracellular metabolic microenvironments (e.g., lactate accumulation) to impact tumor cell metabolic adaptability. Intriguingly, although TREM1 exhibits limited significance in single-gene analyses, it may serve as a critical hub within the"immune-metabolic interactome."Thus, TREM1's pleiotropic functions in immune-metabolic crosstalk provide novel perspectives for understanding the pathogenesis of ovarian tumors.

However, our study still has several limitations. Although we integrated ovarian cancer samples from TCGA, GEO, and ICGC databases, the sample size remains insufficient to comprehensively resolve the high heterogeneity of ovarian cancer subtypes (such as clear cell carcinoma and mucinous carcinoma). The overrepresentation of high-grade serous carcinoma (HGSC) in TCGA cohorts might bias the metabolic pathway analysis toward subtype-specific features of HGSC. Furthermore, the rationality of using immortalized ovarian surface epithelial cells (IOSE) as normal controls is challenged by the emerging"tubal origin hypothesis"in recent years, though current evidence suggests this hypothesis has not yet completely replaced traditional models [49–51]. More importantly, while we bioinformatically inferred correlations between tumor metabolism and immune microenvironment, there is a lack of functional experimental validation regarding the direct regulatory effects of metabolites on immune cells. The bulk sequencing-based analysis cannot distinguish cellular origins of metabolic alterations, thereby neglecting the dynamic heterogeneity of metabolic-immune interactions within tumor spatial contexts. Therefore, considering these limitations mentioned above, future research will employ single-cell transcriptomics and spatial metabolomics to resolve how intratumoral heterogeneity regulates metabolic-immune crosstalk. We will also utilize organoid models or patient-derived primary cells to precisely investigate metabolic adaptation mechanisms during early ovarian cancer evolution.

Conclusion

In summary, the AUCell scoring was applied to identify the highest-scoring monocytes from the OC-related scRNA data. Afterward, two monocyte subpopulations were identified: C1QC$^+$ TAMs and FCN1$^+$ RTMs using gene sets associated with four metabolism processes in OC (choline metabolism, glycolysis metabolism, lipid metabolism, and sphingolipid metabolism). Subsequently, an MRG-based prognostic model was established based on the marker genes for C1QC$^+$ TAMs and

FCN1$^+$ RTMs from the Bulk RNA-seq data. The mRNA expression, CNV, methylation, and SNV were examined at a pan-cancer level using the prognostic model gene set. The prognostic model gene set was further used to assess the high and low risks in patients with OC, which characterized the IME and anti-tumor immune activity in HRG and LRG. Furthermore, the research predicted potential therapeutic drugs for OC and found that angiotensin II receptor antagonists, such as candesartan and PD-123319, may be potential drugs for OC treatment, both of which targeted the *ATGR2* gene. The prognostic significance of the *TREM1* gene was also validated in the prognostic model gene set through in vitro and in vivo experiments, indicating that *TREM1* may serve as an effective independent prognostic biomarker for patients with OC.

Acknowledgements
Graphical Abstract Was Created With Biorender.com.

Authors' contributions
The study conception and design were contributed to by all authors. Lele Ling, Bingrong Li, Boliang Ke, Yinjie Hu, Kaiyong Zhang and Siwen Li were responsible for material preparation, data collection, and analysis. The initial draft of the manuscript was composed by Te Liu, Peng Liu and Bimeng Zhang, with all authors providing feedback on previous iterations. The final manuscript was reviewed and approved by all authors.

Funding
Not applicable.

Data availability
The processed data are available from the corresponding authors upon request.

Declarations

Ethics approval and consent to participate
Ethical approval of this animal experiment was granted by the Experimental Animal Center of Shanghai General Hospital affiliated to Shanghai Jiao Tong University School of Medicine.

Consent for publication
Not applicable.

Competing interests
The authors declare no competing interests.

Author details
[1]Department of Acupuncture, Shanghai General Hospital, Shanghai Jiao Tong University School of Medicine, 100 Haining Road, Shanghai 200086, China. [2]Department of Obstetrics and Gynecology, Shanghai Jiao Tong University Affiliated Sixth People's Hospital, Shanghai Jiao Tong University School of Medicine, Shanghai 200233, China. [3]Shanghai Geriatric Institute of Chinese Medicine, Shanghai University of Traditional Chinese Medicine, 365 South Xiangyang Road, Shanghai 200031, China. [4]School of Health Science and Engineering, University of Shanghai for Science and Technology, Shanghai 200093, China. [5]Department of Urology, Shanghai General Hospital, Shanghai Jiao Tong University School of Medicine, Shanghai 200080, China.

Received: 19 March 2024 Accepted: 22 April 2025
Published online: 17 May 2025

References

1. Colic E, Patel PU, Kent OA. Aberrant MAPK Signaling Offers Therapeutic Potential for Treatment of Ovarian Carcinoma. Onco Targets Ther. 2022;15:1331–46.
2. Zhao H, Teng Y, Hao W, Li J, Li Z, Chen Q, et al. Single-cell analysis revealed that IL4I1 promoted ovarian cancer progression. J Transl Med. 2021;19(1):454.
3. Miller DS, Blessing JA, Krasner CN, Mannel RS, Hanjani P, Pearl ML, et al. Phase II evaluation of pemetrexed in the treatment of recurrent or persistent platinum-resistant ovarian or primary peritoneal carcinoma: a study of the Gynecologic Oncology Group. J Clin Oncol. 2009;27(16):2686–91.
4. Kumaran GC, Jayson GC, Clamp AR. Anti-angiogenic drugs in ovarian cancer. Br J Cancer. 2009;100(1):1–7.
5. Jin C, Yuan M, Bu H, Jin C. Anti-angiogenic Strategies in Epithelial Ovarian Cancer: Mechanism, Resistance, and Combination Therapy. J Oncol. 2022;2022:4880355.
6. Jayson GC, Kerbel R, Ellis LM, Harris AL. Anti-angiogenic therapy in oncology: current status and future directions. Lancet. 2016;388(10043):518–29.
7. Park M, Choe S, Shin M, Kim A, Mo K, Kwon H, et al. Potential Therapeutic Targets in Ovarian Cancer: Autophagy and Metabolism. Front Biosci (Landmark Ed). 2023;28(3):47.
8. Pavlova NN, Zhu J, Thompson CB. The hallmarks of cancer metabolism: Still emerging. Cell Metab. 2022;34(3):355–77.
9. Hanahan D, Weinberg RA. Hallmarks of cancer: the next generation. Cell. 2011;144(5):646–74.
10. Faubert B, Solmonson A, DeBerardinis RJ. Metabolic reprogramming and cancer progression. Science. 2020;368(6487):eaaw5473.
11. Ahmed N, Escalona R, Leung D, Chan E, Kannourakis G. Tumour microenvironment and metabolic plasticity in cancer and cancer stem cells: Perspectives on metabolic and immune regulatory signatures in chemoresistant ovarian cancer stem cells. Semin Cancer Biol. 2018;53:265–81.
12. Yu T-J, Ma D, Liu Y-Y, Xiao Y, Gong Y, Jiang Y-Z, et al. Bulk and single-cell transcriptome profiling reveal the metabolic heterogeneity in human breast cancers. Mol Ther. 2021;29(7):2350–65.
13. Liu J, Lichtenberg T, Hoadley KA, Poisson LM, Lazar AJ, Cherniack AD, et al. An Integrated TCGA Pan-Cancer Clinical Data Resource to Drive High-Quality Survival Outcome Analytics. Cell. 2018;173(2):400-416.e11.
14 Hao Y, Hao S, Andersen-Nissen E, Mauck WM, Zheng S, Butler A, et al. Integrated analysis of multimodal single-cell data. Cell. 2021;184(13):3573-3587.e29.
15. Aran D, Looney AP, Liu L, Wu E, Fong V, Hsu A, et al. Reference-based analysis of lung single-cell sequencing reveals a transitional profibrotic macrophage. Nat Immunol. 2019;20(2):163–72.
16. Aibar S, González-Blas CB, Moerman T, Huynh-Thu VA, Imrichova H, Hulselmans G, et al. SCENIC: single-cell regulatory network inference and clustering. Nat Methods. 2017;14(11):1083–6.
17 Liu Y, Zhang Q, Xing B, Luo N, Gao R, Yu K, et al. Immune phenotypic linkage between colorectal cancer and liver metastasis. Cancer Cell. 2022;40(4):424-437.e5.
18. Chen B, Khodadoust MS, Liu CL, Newman AM, Alizadeh AA. Profiling Tumor Infiltrating Immune Cells with CIBERSORT. Methods Mol Biol. 2018;1711:243–59.
19. Kawada J-I, Takeuchi S, Imai H, Okumura T, Horiba K, Suzuki T, et al. Immune cell infiltration landscapes in pediatric acute myocarditis analyzed by CIBERSORT. J Cardiol. 2021;77(2):174–8.
20. Mayakonda A, Lin D-C, Assenov Y, Plass C, Koeffler HP. Maftools: efficient and comprehensive analysis of somatic variants in cancer. Genome Res. 2018;28(11):1747–56.
21. Zhou X, Lin K, Fu L, Liu F, Lin H, Chen Y, et al. Overexpression of TREM1 is Associated with the Immune-Suppressive Microenvironment and Unfavorable Prognosis in Pan-Cancer. J Inflamm Res. 2023;16:1375–91.
22. Zhong W-J, Liu T, Yang H-H, Duan J-X, Yang J-T, Guan X-X, et al. TREM-1 governs NLRP3 inflammasome activation of macrophages by firing up glycolysis in acute lung injury. Int J Biol Sci. 2023;19(1):242–57.
23. Sung H, Ferlay J, Siegel RL, Laversanne M, Soerjomataram I, Jemal A, et al. Global Cancer Statistics 2020: GLOBOCAN Estimates of Incidence and Mortality Worldwide for 36 Cancers in 185 Countries. CA Cancer J Clin. 2021;71(3):209–49.
24. Colombo N, Sessa C, du Bois A, Ledermann J, McCluggage WG, McNeish I, et al. ESMO-ESGO consensus conference recommendations on ovarian cancer: pathology and molecular biology, early and

advanced stages, borderline tumours and recurrent disease†. Ann Oncol. 2019;30(5):672–705.
25. Pavlova NN, Thompson CB. The Emerging Hallmarks of Cancer Metabolism. Cell Metab. 2016;23(1):27–47.
26. Vander Heiden MG, Cantley LC, Thompson CB. Understanding the Warburg effect: the metabolic requirements of cell proliferation. Science. 2009;324(5930):1029–33.
27. Wang M, Zhang J, Wu Y. Tumor metabolism rewiring in epithelial ovarian cancer. J Ovarian Res. 2023;16(1):108.
28. Bagnoli M, Granata A, Nicoletti R, Krishnamachary B, Bhujwalla ZM, Canese R, et al. Choline Metabolism Alteration: A Focus on Ovarian Cancer. Front Oncol. 2016;6:153.
29. Granata A, Nicoletti R, Tinaglia V, De Cecco L, Pisanu ME, Ricci A, et al. Choline kinase-alpha by regulating cell aggressiveness and drug sensitivity is a potential druggable target for ovarian cancer. Br J Cancer. 2014;110(2):330–40.
30. Kreitzburg KM, van Waardenburg RCAM, Yoon KJ. Sphingolipid metabolism and drug resistance in ovarian cancer. Cancer Drug Resist. 2018;1:181–97.
31. Levine AJ, Puzio-Kuter AM. The control of the metabolic switch in cancers by oncogenes and tumor suppressor genes. Science. 2010;330(6009):1340–4.
32. Cairns RA. Drivers of the Warburg phenotype. Cancer J. 2015;21(2):56–61.
33. Teicher BA, Linehan WM, Helman LJ. Targeting cancer metabolism. Clin Cancer Res. 2012;18(20):5537–45.
34. Smith B, Schafer XL, Ambeskovic A, Spencer CM, Land H, Munger J. Addiction to Coupling of the Warburg Effect with Glutamine Catabolism in Cancer Cells. Cell Rep. 2016;17(3):821–36.
35. Naeini MB, Momtazi AA, Jaafari MR, Johnston TP, Barreto G, Banach M, et al. Antitumor effects of curcumin: A lipid perspective. J Cell Physiol. 2019;234(9):14743–58.
36. Martano M, Power K, Cuccaro B, Razzuoli E, Maiolino P, Restucci B. Overexpression of the key metabolic protein Carnitine Palmitoyl Transferase 1A (CPT1A) in equine sarcoid. J Equine Vet Sci. 2024;143:105205.
37. Kelly W, Diaz Duque AE, Michalek J, Konkel B, Caflisch L, Chen Y, et al. Phase II Investigation of TVB-2640 (Denifanstat) with Bevacizumab in Patients with First Relapse High-Grade Astrocytoma. Clin Cancer Res. 2023;29(13):2419–25.
38. Chen C, Wang Z, Qin Y. Connections between metabolism and epigenetics: mechanisms and novel anti-cancer strategy. Front Pharmacol. 2022;13:935536.
39. Treglia G, Giovannini E, Di Franco D, Calcagni ML, Rufini V, Picchio M, et al. The role of positron emission tomography using carbon-11 and fluorine-18 choline in tumors other than prostate cancer: a systematic review. Ann Nucl Med. 2012;26(6):451–61.
40. Kall SL, Delikatny EJ, Lavie A. Identification of a Unique Inhibitor-Binding Site on Choline Kinase α. Biochemistry. 2018;57(8):1316–25.
41. Cuyàs E, Fernández-Arroyo S, Joven J, Menendez JA. Metformin targets histone acetylation in cancer-prone epithelial cells. Cell Cycle. 2016;15(24):3355–61.
42. Okazaki M, Fushida S, Harada S, Tsukada T, Kinoshita J, Oyama K, et al. The angiotensin II type 1 receptor blocker candesartan suppresses proliferation and fibrosis in gastric cancer. Cancer Lett. 2014;355(1):46–53.
43. Tabatabai E, Khazaei M, Asgharzadeh F, Nazari SE, Shakour N, Fiuji H, et al. Inhibition of angiotensin II type 1 receptor by candesartan reduces tumor growth and ameliorates fibrosis in colorectal cancer. EXCLI J. 2021;20:863–78.
44. Fan F, Tian C, Tao L, Wu H, Liu Z, Shen C, et al. Candesartan attenuates angiogenesis in hepatocellular carcinoma via downregulating AT1R/VEGF pathway. Biomed Pharmacother. 2016;83:704–11.
45. Nakai Y, Isayama H, Ijichi H, Sasaki T, Kogure H, Yagioka H, et al. Phase I trial of gemcitabine and candesartan combination therapy in normotensive patients with advanced pancreatic cancer: GECA1. Cancer Sci. 2012;103(8):1489–92.
46. Busby J, McMenamin Ú, Spence A, Johnston BT, Hughes C, Cardwell CR. Angiotensin receptor blocker use and gastro-oesophageal cancer survival: a population-based cohort study. Aliment Pharmacol Ther. 2018;47(2):279–88.
47. Zysset D, Weber B, Rihs S, Brasseit J, Freigang S, Riether C, et al. TREM-1 links dyslipidemia to inflammation and lipid deposition in atherosclerosis. Nat Commun. 2016;7:13151.
48. Wu Q, Zhou W, Yin S, Zhou Y, Chen T, Qian J, et al. Blocking Triggering Receptor Expressed on Myeloid Cells-1-Positive Tumor-Associated Macrophages Induced by Hypoxia Reverses Immunosuppression and Anti-Programmed Cell Death Ligand 1 Resistance in Liver Cancer. Hepatology. 2019;70(1):198–214.
49. McCluggage WG, Hirschowitz L, Gilks CB, Wilkinson N, Singh N. The Fallopian Tube Origin and Primary Site Assignment in Extrauterine High-grade Serous Carcinoma: Findings of a Survey of Pathologists and Clinicians. Int J Gynecol Pathol. 2017;36(3):230–9.
50. Singh N, Gilks CB, Wilkinson N, McCluggage WG. The secondary Müllerian system, field effect, BRCA, and tubal fimbria: our evolving understanding of the origin of tubo-ovarian high-grade serous carcinoma and why assignment of primary site matters. Pathology. 2015;47(5):423–31.
51. Greenwood A, Woodruff ER, Nguyen C, Piper C, Clauset A, Brubaker LW, et al. Early Ovarian Cancer Detection in the Age of Fallopian Tube Precursors: A Systematic Review. Obstet Gynecol. 2024;143(3):e63–77.

Publisher's Note